Cascade of magnetic transitions in the frustrated antiferromagnetic CePtPb

by

Alex Ching-Yang Fang

B.Sc., University of British Columbia, 2016

Thesis Submitted in Partial Fulfillment of the
Requirements for the Degree of
Master of Science

in the
Department of Physics
Faculty of Science

Approval

Name: **Alex Ching-Yang Fang**

Degree: **Master of Science (Physics)**

Title: **Cascade of magnetic transitions in the frustrated antiferromagnetic CePtPb**

Examining Committee: **Chair:** Malcolm Kennett
Associate Professor

Jeff Sonier
Senior Supervisor
Professor

Eundeok Mun
Supervisor
Assistant Professor

David Broun
Internal Examiner
Associate Professor

Date Defended: **August 8, 2018**

Abstract

CePtPb is an antiferromagnetic, heavy-fermion, metallic compound that crystallizes in the ZrNiAl-type structure with space group P$\bar{6}$2m, where the Ce^{3+}-ions form a quasi-Kagome lattice in the ab-plane. Other compounds in this family with a quasi-Kagome magnetic lattice such as CePdAl and YbAgGe have shown a complex temperature-versus-magnetic field (T-H) phase diagram with multiple magnetically-ordered phases. In this thesis, a T-H phase diagram for single crystal CePtPb is constructed from electric resistivity and specific heat measurements. The constructed phase diagram also shows multiple magnetically-ordered phases as the Néel temperature $T_{\mathrm{N}} \approx 0.9$ K is suppressed continuously to $T = 0.4$ K by applied field with an extrapolated zero-temperature critical field $H_{\mathrm{c}} \approx 7$ kOe. In zero-field, muon spin relaxation measurements show residual spin dynamics at 25 mK, consistent with the magnetic structure proposed for CePdAl, where 2/3 of the Ce-4f spins order antiferromagnetically and the other 1/3 of the Ce-4f spins remain fluctuating. From a power-law analysis of the electrical resistivity ($\rho = \rho_0 + AT^n$), neither Fermi-liquid ($n = 2$) nor non-Fermi-liquid ($n < 2$) behaviour have been observed down to $T = 0.4$ K for $H \geq H_{\mathrm{c}}$. Instead, there is an anomalous evolution of n that increases from $n = 2.5$ at $H = H_{\mathrm{c}}$ to $n = 4.1$ at $H = 90$ kOe, with a tendency towards saturation near the value $n \approx 4$ for $H > 30$ kOe. The phase diagram and the measurements are compared to CePdAl and YbAgGe.

Keywords: heavy-fermion, geometric frustration, quantum critical point, μSR

Dedication

To the young and naive me

Acknowledgements

Table of Contents

List of Tables

List of Figures

x

Chapter 1

Introduction

Heavy-fermion compounds are a class of materials with rare-earth or actinide elements that have partially filled $4f$- or $5f$-electron shells. The term "heavy-fermion" refers to the effective mass m^* of the conduction electrons in these compounds, which is orders of magnitude greater than the free-electron mass. The large effective mass affects the coefficients of the electronic contribution to the electrical resistivity ($\rho \sim AT^2$) and the specific heat ($C_\mathrm{p} \sim \gamma T$), which are also orders of magnitude greater than that of normal metals. For copper, the electronic specific heat (Sommerfeld) coefficient is $\gamma \approx 0.7$ mJ/mol K^2 [1] and the resistivity coefficient is $A = 2 \times 10^{-8}$ $\mu\Omega$ cm/K^2 [2], whereas for a well known heavy-fermion compound, CeAl$_3$, the coefficients are $\gamma = 1620$ mJ/mol K^2 [3] and $A = 35$ $\mu\Omega$ cm/K^2 [4].

The large effective mass originates from screening of the localized f-electron magnetic moments by the conduction electrons through the so-called "Kondo effect". The Kondo effect tends to drive the system toward a paramagnetic ground state by fully screening the f-electron moments. On the other hand, another important interaction in heavy-fermion compounds, the Ruderman-Kittel-Kasuya-Yosida (RKKY) interaction, tends to favour a magnetic ground state. The RKKY interaction is an indirect coupling between the localized f-electron spins mediated by the conduction electrons. Depending on the relative strength of the Kondo effect compared to the RKKY interaction, heavy-fermion compounds exhibit various phenomena, including long-range magnetic order [5], valence fluctuations [6], and unconventional superconductivity [7, 8, 9].

Doniach proposed that heavy-fermion compounds evolve from a dense lattice version of the Kondo effect [10]. A sub-class of heavy-fermion metals develop an antiferromagnetic (AFM) state at low temperatures due to a dominant RKKY interaction. In Doniach's model, the AFM transition temperature (or Néel temperature) T_N is continuously suppressed to zero by increasing the exchange coupling J between the f-electron and conduction electron spins. At some critical coupling value J_c, T_N is fully suppressed to zero at an AFM quantum critical point (QCP). The transition at the QCP is believed to be driven by quantum critical fluctuations of the f-electron spins. A driving force for these fluctuations is Heisenberg's uncertainty principle, which allows for zero-point (zero-temperature) fluctuations of the

spins. With a further increase in J beyond J_c, the localized f-electron moments become fully screened and the compound develops a Fermi-liquid ground state. Experimentally, the exchange coupling J can be modified by a non-thermal tuning parameter (g), such as chemical doping (x), applied pressure (p), or applied magnetic field (H). The quantum critical fluctuations give rise to a sub-quadratic resistivity and a magnetic contribution to the specific heat that exhibits a $-\log T$ temperature dependence. Such behaviours are signatures of a non-Fermi liquid (NFL).

Several compounds, including $CeCu_{6-x}Au_x$ [11], $YbRh_2Si_2$ [12], $CeIn_3$ [7, 8, 9], and $CePd_2Si_2$ [7] exhibit NFL behaviour near a QCP when AFM order is suppressed by a tuning parameter, which is in agreement with Doniach's model. However, recent studies of another compound in the heavy-fermion class, YbAgGe [13, 14, 15, 16, 17, 18], have found multiple AFM phases before arriving at a QCP. Moreover, an anomalous phase with NFL behaviour has been observed near the QCP [13, 16]. These findings suggest that Doniach's model may be incomplete.

An extension of the Doniach model is the inclusion of magnetic frustration, which arises naturally in some heavy-fermion compounds. Typically, the magnetic frustration has a geometric origin, where the interactions between nearest-neighbour or next-nearest neighbour spins are competing with one another. Magnetically frustrated compounds have been shown to have novel ground states, such as spiral AFM order in $CeRhIn_5$ [19, 20] and spin ice behaviour in $Dy_2Ti_2O_7$ [21].

In YbAgGe and CePdAl, the rare-earth ions form a quasi-Kagome lattice in the *ab*-plane [Fig. 1.7(a)] resulting in geometrical magnetic frustration. While YbAgGe exhibits NFL behaviour when the AFM order is suppressed by an applied magnetic field, CePdAl [22] does not exhibit NFL behaviour when the AFM order is suppressed with field. In this context, it is interesting to explore the quantum critical behaviour of CePtPb by tuning with applied magnetic fields, because it is a related compound with Ce-4f spins arranged in a quasi-Kagome lattice. Henceforth the focus of this thesis will be on the family of heavy-fermion compounds that are AFM metals.

1.1 Kondo Effect

The Kondo effect refers to the screening of the localized electronic magnetic moments by the spins of the conduction electrons. In 1964, Kondo derived the effect on the electrical resistivity via a third-order perturbative calculation within the framework of a *s-d* model for a single spin-1/2 magnetic impurity [23]. A schematic for the derived temperature dependence of the Kondo contribution to the electrical resistivity $\rho(T)$ is shown in Fig. 1.1(a). $\rho(T)$ exhibits a $-\log T$ temperature dependence above a characteristic (Kondo) temperature T_K and saturates at temperatures below T_K. The temperature dependence of the Kondo contribution to the magnetic susceptibility and specific heat were later derived [24].

Schematics of these behaviours are also shown in Fig. 1.1(a). The derived Kondo contribution to the magnetic susceptibility follows a Curie-Weiss law $\chi(T) = C/(T - \theta_{\mathrm{CW}})$ for $T \gg T_{\mathrm{K}}$, where C is the Curie constant that depends on the concentration of localized magnetic impurity moments and θ_{CW} is the Curie-Weiss temperature. In the $T \ll T_{\mathrm{K}}$ limit, the magnetic impurity moment is fully screened by the conduction electrons and χ is due to the finite and temperature-independent Pauli paramagnetic susceptibility. On the other hand, the derived Kondo contribution to the specific heat C_{p} develops a T-linear temperature dependence in the $T \ll T_{\mathrm{K}}$ limit. A broad peak is observed as the temperature is increased towards T_{K} with the area under the peak corresponding to a spin entropy change of $R \ln 2$, where R is the ideal gas constant. It is important to emphasize that T_{K} is not a phase transition temperature, but rather is the crossover energy scale below which the local moment is asymptotically screened.
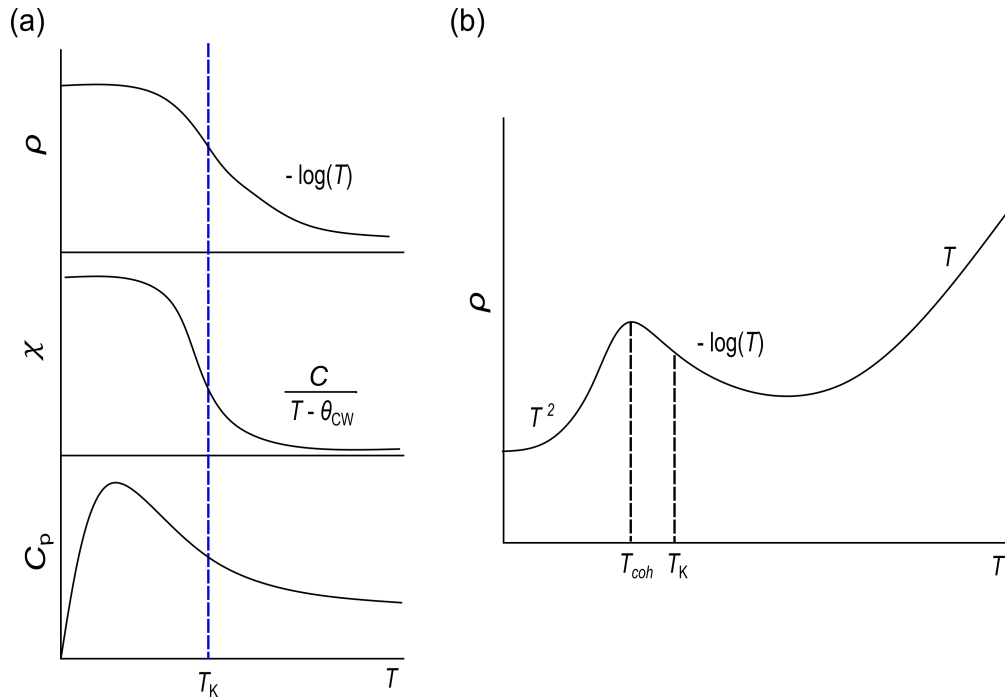
Figure 1.1: (a) Schematic of Kondo contribution to the electrical resistivity ρ, magnetic susceptibility χ, and specific heat C_{p} in the single-ion Kondo model with a spin-1/2 impurity. (b) The typical temperature dependence of the electrical resistivity for a Kondo lattice system.

The reason Kondo derived this impurity contribution to the electrical conductivity was to explain the resistivity minimum and the $-\log T$ temperature dependence at lower temperatures observed in compounds with dilute d- or f-electron impurity spins [25, 26, 27]. The resistivity minimum was explained as the consequence of the decreasing phonon contribution ($\propto T$) and the growing Kondo contribution ($\propto -\log T$) as temperature is decreased.

In dense magnetic (Kondo lattice) systems [Fig. 1.1(b)], $\rho(T)$ exhibits a local maximum at a temperature below T_{K} and $\rho(T)$ follows a T^2 dependence at lower temperature. This cannot be explained by the single-ion Kondo model, but rather a periodic Anderson model [28] needs to be considered. This model introduces another crossover temperature, T_{coh}. Below T_{coh} the system is a Kondo lattice with fully screened f-electron spins that exhibit Fermi-liquid behaviour ($\propto T^2$) [29]. Above T_{coh}, the interaction between the f-electron spins is weak, so that they can be treated as a collection of incoherent magnetic impurities. In this case, a minimum and a $-\log T$ temperature dependence of the electrical resistivity occur above T_{coh}, similar to the single-ion picture.

1.2 RKKY Interactions

The Ruderman-Kittel-Kasuya-Yosida (RKKY) interaction is an indirect magnetic exchange interaction between the localized f-electron spins mediated by the conduction electrons. The localized magnetic moment $\langle \mathbf{S}\,(\mathbf{x}') \rangle$ of an f-electron at position $\mathbf{x}'$ creates a wave of Friedel oscillations [Fig. 1.2] in the conduction electron spin density $\langle \sigma(\mathbf{x}) \rangle$, such that

$$\langle \boldsymbol{\sigma}(\mathbf{x}) \rangle = J\chi(\mathbf{x} - \mathbf{x}')\langle \mathbf{S}(\mathbf{x}') \rangle \tag{1.1}$$

where $\chi(\mathbf{x} - \mathbf{x}')$ is the non-local magnetic susceptibility and J is the AFM coupling [29]. The spin density oscillation arises from the sharp discontinuity in the occupancies $f(\epsilon_{\mathrm{k}})$ at the Fermi surface and decays radially as follows

$$\langle \boldsymbol{\sigma}(\mathbf{x}) \rangle \sim -JD\frac{\cos 2k_{\mathrm{F}}x}{|k_{\mathrm{F}}x|^3} \tag{1.2}$$

where D is the conduction electron density of states and x is the distance from the magnetic moment. When a second local moment $\langle \boldsymbol{S}(\mathbf{x}) \rangle$ is placed at $\mathbf{x}$, it couples to the Friedel oscillation with energy $J\langle \mathbf{S}(\mathbf{x}) \cdot \boldsymbol{\sigma}(\mathbf{x}) \rangle$. Using Eq. (1.1), this gives the famous RKKY Hamiltonian

$$\begin{aligned} H_{\mathrm{RKKY}} &= J\langle \mathbf{S}(\mathbf{x}) \cdot \boldsymbol{\sigma}(\mathbf{x}) \rangle \\ &= -J^2\chi(\mathbf{x} - \mathbf{x}')\mathbf{S}(\mathbf{x}) \cdot \mathbf{S}(\mathbf{x}') \\ &\equiv J_{\mathrm{RKKY}}(\mathbf{x} - \mathbf{x}')\mathbf{S}(\mathbf{x}) \cdot \mathbf{S}(\mathbf{x}') \end{aligned} \tag{1.3}$$

where $J_{\mathrm{RKKY}}(\mathbf{x} - \mathbf{x}') = J_{\mathrm{RKKY}}(r) \sim -J^2D\cos(2k_{\mathrm{F}}r)/k_{\mathrm{F}}r$ [30, 31, 32]. Note that r is the distance between a local moment sitting at $\mathbf{x}$ and another local moment sitting at $\mathbf{x}'$. In alloys that contain a dilute concentration of magnetic rare-earth or transition metal ions, the RKKY interaction between magnetic ions with random positions can give rise to a random distribution of AFM and ferromagnetic (FM) interactions. The magnetic state that arises from the disorder and frustration is a "spin glass". In a spin-glass state, the localized spins are frozen into random orientations. On the other hand, a dense system of magnetic ions

often results in an AFM (or FM) state with a Néel temperature T_N (or Curie temperature T_C) on the order of $J^2 D$.
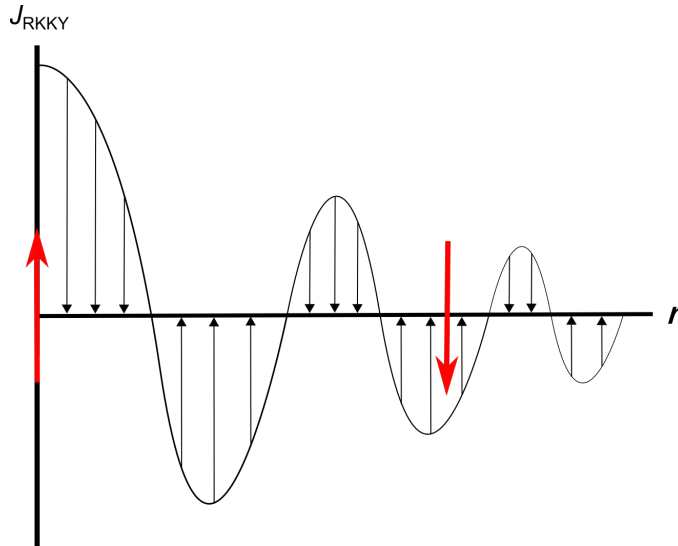
Figure 1.2: Schematic of an RKKY interaction. A localized f-electron magnetic moment (red arrow) at the origin induces Friedel oscillations in the surrounding conduction electron spin density. Another localized f-moment some distance away couples to the Friedel oscillation with strength J_RKKY.

1.3 Quantum Criticality

As mentioned earlier, the consequences of the relative strength of the Kondo effect and RKKY interaction in AFM heavy-fermion metals are qualitatively described by the so-called "Doniach phase diagram" [10] in terms of the AFM coupling J between the f-electron and conduction electron spins. A schematic of this phase diagram is presented in Fig. 1.3, which is adopted from [33]. In the Doniach phase diagram, the characteristic temperatures of the single-ion Kondo effect and the RKKY interaction are given by

$$T_\mathrm{K} \propto e^{-1/JD(E_\mathrm{F})} \tag{1.4}$$

$$T_\mathrm{RKKY} \propto J^2 D(E_\mathrm{F}) \tag{1.5}$$

where $D(E_\mathrm{F})$ is the conduction electron density of states at the Fermi energy E_F.

In the $T_\mathrm{K} \gg T_\mathrm{RKKY}$ regime, the local f-electron spins are fully screened by the conduction electrons and the system forms a heavy Fermi liquid. In the opposite limit, where $T_\mathrm{K} \ll T_\mathrm{RKKY}$, an AFM state occurs with a Néel temperature T_N that tracks T_RKKY with a J^2 dependence. Since T_K increases more rapidly than T_RKKY with increasing J, there is an intermediate value of J where T_N reaches a maximum. At higher J values, T_N is suppressed
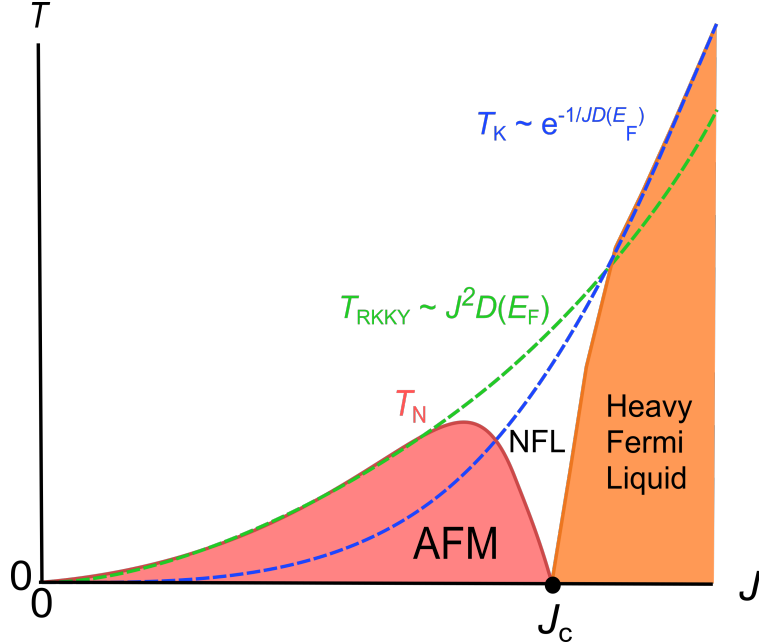
Figure 1.3: Doniach phase diagram for heavy-fermion metals. The dashed curves represent the dependence of the Kondo and RKKY characteristic temperatures, T_K and T_{RKKY}, on the effective AFM coupling J between the localized f-electron and conduction electron spins. The parameter $D(E_F)$ is the conduction electron density of states at the Fermi energy.

continuously to zero at a critical coupling value J_c, where the Kondo and RKKY interactions are comparable. The zero-temperature transition between the AFM and the paramagnetic heavy Fermi-liquid states is a quantum critical point (QCP). This phase transition is driven by quantum critical fluctuations, which result in the system exhibiting non-Fermi liquid behaviour (NFL) near the QCP [34, 35].

Figure 1.4 shows a generic T versus g phase diagram for an AFM heavy-fermion system. The Néel temperature T_N of the AFM state is suppressed continuously to a QCP at a critical tuning value $g = g_c$. For $g > g_c$, Fermi liquid behaviour is observed. Near $g = g_c$, NFL behaviour is observed as a sub-quadratic electrical resistivity and a $-\log T$ or $-\sqrt{T}$ temperature dependence of the magnetic contribution to the specific heat [34, 35]. The specific temperature dependence of these measurements depends on the dimensionality and the type of magnetic ordering of the system, as well as the particular spin-fluctuation theory considered [36, 37, 38]. These temperature dependences have been observed in numerous Ce- and Yb-based $4f$-electron systems. Some examples are doping-tuned $CeCu_{6-x}Au_x$ [11], pressure-tuned $CePd_2Si_2$ [7] and $CeIn_3$ [7, 8, 9], and magnetic-field-tuned $YbRh_2Si_2$ [12] and YbAgGe [13]. In $CeIn_3$ [7, 8, 9] and $CePd_2Si_2$ [7], unconventional superconductivity is observed near the QCP. In YbAgGe [13], $CeAuSb_2$ [39], and CePdAl [22], the coefficient A of the electronic contribution to the electrical resistivity, which exhibits T^2 behaviour, has
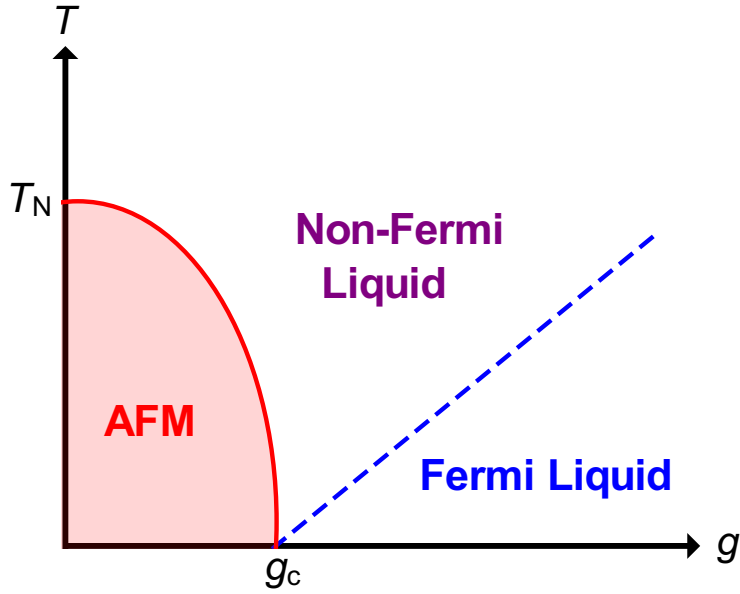
Figure 1.4: Generic phase diagram that is typically presented for AFM heavy-fermion compounds, showing the continuous suppression of the Néel temperature T_N by a tuning parameter g.

been observed to diverge when the QCP is approached from the Fermi-liquid side of the T-g phase diagram.

1.4 Magnetic Frustration

Magnetic frustration arises naturally in various compounds and can result in quantum zero-point fluctuation of spins. Magnetic frustration refers to the presence of competing magnetic interactions that can't be simultaneously satisfied. In an antiferromagnet, this frustration typically has a geometric origin [40]. To illustrate this, consider a two-dimensional edge-sharing triangular lattice with Ising spins that are AFM coupled in the plane, as shown in Fig. 1.5(a). For each triangle, there is at least one spin that can't perfectly satisfy all of the AFM interactions with its neighbours. This simple lattice was shown by Wannier [41] to have a large ground-state degeneracy, with a non-zero entropy $S(0) = 0.3383R$ at zero temperature, where R is the ideal-gas constant. This has also been shown to be the case for a two-dimensional Kagome lattice, which is a corner-sharing triangular lattice characteristic of YbAgGe and CePtPb [42]. In this case, there is a larger residual entropy of $S(0) = 0.5018R$.

Magnetic frustration profoundly influences the ground state. In tetragonal CeRhIn$_5$, a spiral AFM ground state occurs due to frustration that arises from competing RKKY in-
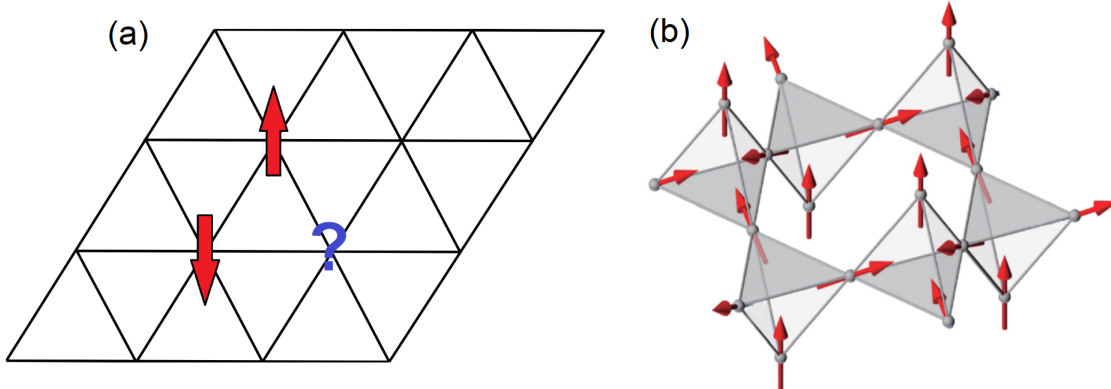
Figure 1.5: (a) Triangular lattice with in-plane Ising spins that couple antiferromagnetically, showing the geometric magnetic frustration that occurs across each triangle. (b) Corner-sharing tetrahedral lattice of a spin-ice compound, showing the "two-in-two-out" ice rule for the spins across each tetrahedron. This figure is taken from [43], which is modified from [44].

teractions between nearest-neighbour and next-nearest neighbour Ce-$4f$ magnetic moments [19, 20]. In the pyrochlore spin-ice compound $Dy_2Ti_2O_7$, although the exchange interaction between the nearest-neighbour Dy ions are AFM, there are still net FM interactions between them due to the magnetic dipolar field they experience from their neighbours and the geometry of the corner-sharing tetrahedral lattice they sit on. The combination of FM interactions between spins on a pyrochlore lattice with strong $\langle 111 \rangle$ anisotropy give rise to frustration that results in a "two-in-two-out" spin configuration across each tetrahedron, as shown in Fig. 1.5(b) [21]. In the extreme case, strong frustration can lead to exotic spin liquid-like behaviour at zero temperature (i.e., a "quantum-spin" liquid state). In contrast to a paramagnetic state, the randomly fluctuating spins of the quantum spin liquid are strongly correlated and potentially phase coherent [40].

The degree of magnetic frustration in insulating systems is typically inferred from the value of the so-called "frustration ratio" $f = \theta_{CW}/T_N$, where the Curie-Weiss temperature θ_{CW} is the theoretical ordering temperature from nearest-neighbour interactions and T_N is the actual AFM transition temperature. For simple systems like MnF_2, f has a value close to 1 [1]. For the case of the frustrated insulating compound α-$RuCl_3$, the value is $f \approx 10$ [45]. In the heavy-fermion metal YbAgGe, f has been calculated to be approximately 30 [15, 13], suggesting a high degree of magnetic frustration. However, it is important to emphasize that in heavy-fermion compounds the value of the frustration ratio may be significantly influenced by the Kondo effect and crystal electric field (CEF) effect.

Figure 1.6 shows the so called "QK" phase diagram [46] that qualitatively describes the behaviour of a frustrated AFM heavy-fermion system. The Q-axis is a measure of the quantum zero-point motion (e.g. geometric frustration) of the f-spins, while the K-axis
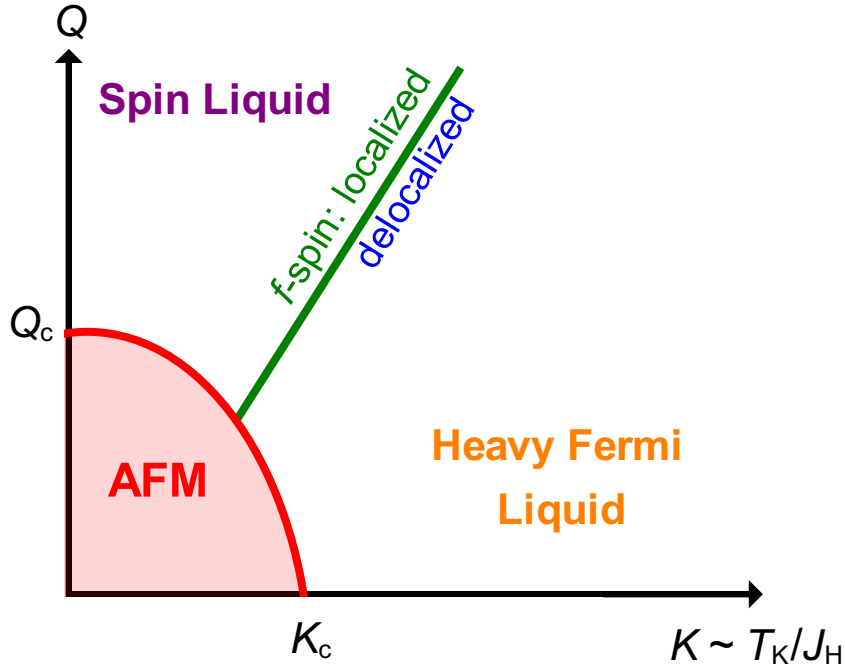
Figure 1.6: Generic phase diagram for magnetically-frustrated AFM heavy-fermion systems.

is a measure of the effect of Kondo screening. This effect is given by the ratio between the characteristic Kondo temperature T_K and the characteristic strength of the short-range AFM Heisenberg interactions J_H between the f-spins. In non-frustrated metals ($Q = 0$), increasing K continuously suppresses the Néel temperature to zero at a critical tuning value K_c and gives rise to heavy Fermi-liquid behaviour with delocalized f-spins for $K > K_c$. On the other hand, by increasing the strength of the quantum zero-point motion of the f-spins in insulating systems ($K \ll 1$), the system develops spin-liquid behaviour when the AFM ordering is suppressed at a critical tuning value Q_c. The f-spins in this case are well-localized and there must be a crossover when the Kondo effect gradually delocalizes the f-spins. There is a continuous critical line that connects K_c and Q_c which separates the AFM phase from the other phases. In general, this phase diagram allows for the classification of various magnetically-frustrated compounds.

1.5 Previous Studies of Frustrated AFM Heavy-Fermion compounds

1.5.1 YbAgGe

As mentioned earlier, the compound YbAgGe is an AFM heavy-fermion metal with the same crystal structure as CePtPb. Each crystallizes in the hexagonal ZrNiAl-type structure
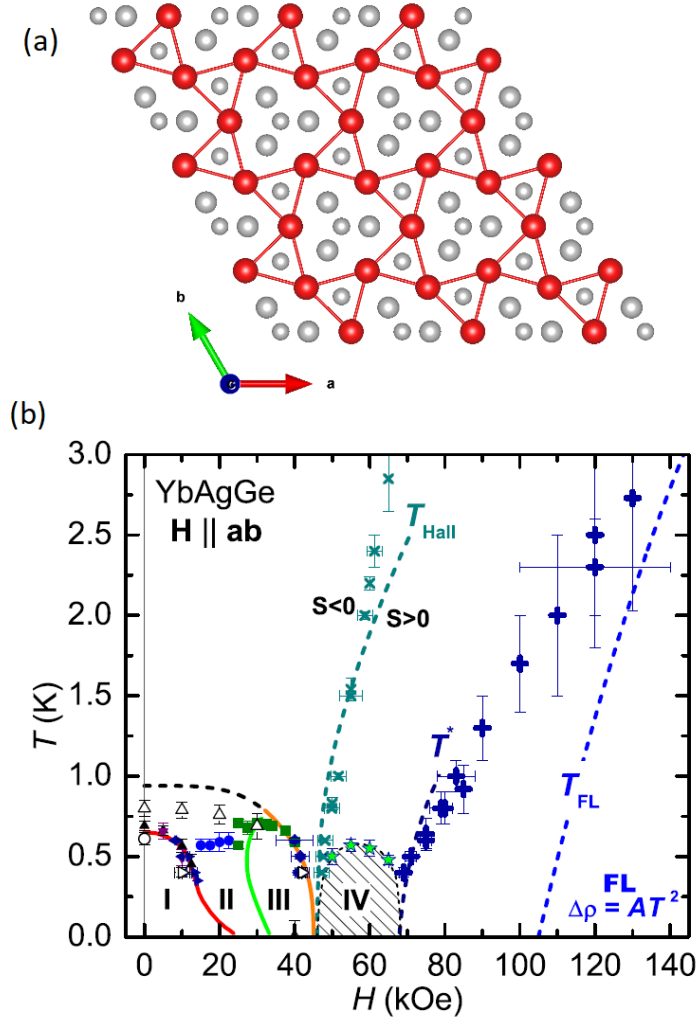
Figure 1.7: (a) Quasi-Kagome lattice of magnetic Yb ions (red) in YbAgGe. (b) Temperature-magnetic field phase diagram of YbAgGe [16].

with a P$\bar{6}$2m space group. As shown in Fig. 1.7(a), the magnetic Yb ions reside at the 3g site, forming a quasi-Kagome lattice in the *ab*-plane. In the absence of an applied magnetic field, YbAgGe is characterized by a Sommerfeld coefficient $\gamma = 150$ mJ/mol K^2, a Kondo temperature $T_K = 25$ K, a first-order AFM transitions at $T_{N,1} \approx 0.65$ K and a second-order AFM transition at $T_{N,2} \approx 1$ K [13, 14, 16]. The reported Curie-Weiss temperature $\theta_{CW} = -30$ K [15] implies a large frustration ratio $f = \theta_{CW}/T_{N,2} = 30$.

A magnetic field applied in the magnetic easy *ab*-plane induces multiple AFM phases [phase I, II, III in Fig. 1.7(b)]. The second-order AFM transition temperature is suppressed to zero at a critical field $H_c \sim 45$ kOe [16, 17]. Phase I is a commensurate AFM phase with a magnetic propagation vector $\mathbf{k}_1 = (1/3, 0, 1/3)$ [47]. Phase II is an incommensurate

10

AFM phase with $\mathbf{k}_2 = (0, 0, 0.324)$, and phase III is a commensurate AFM phase similar to phase 1, but with small staggered moments. Near H_c, an additional unknown phase (IV) is observed in thermodynamic and transport measurements [13, 16]. Phase IV exhibits NFL behaviour, characterized by a T-linear electrical resistivity [i.e., $\rho(T) = \rho_0 + AT^n$, where $n = 1$]. Above $H = 70$ kOe, n varies smoothly from 1 to 2. Fermi liquid behaviour ($n = 2$) is not observed until $H \approx 105$ kOe.

1.5.2 CePdAl

CePdAl is another AFM heavy-fermion metal in which the Ce $4f$ magnetic moments form a Kagome lattice. In zero-field, CePdAl is characterized by a Sommerfeld coefficient ($\gamma = 250$ mJ/mol K^2) [48], Kondo temperature ($T_K \approx 6$ K), Neel temperature ($T_N = 2.7$ K) and the Curie-Weiss temperature ($\theta_{CW} = -34$ K) [49, 50]. The corresponding frustration ratio is $f = \theta_{CW}/T_N = 12.6$. Previous zero-field inelastic neutron scattering [49] and ^{27}Al NMR [51] studies suggest three magnetically inequivalent Ce sites, where two of them couple antiferromagnetically along the magnetic easy c-axis, while the third one remains fluctuating down to zero temperature [as shown in Fig. 1.8(a)]. Based on a symmetry analysis [49], the frustrated Ce spins are prohibited to point along the c-axis. An applied magnetic field along the c-axis has been shown to continuously lift the frustration of the Ce spins up to 3.6 T [52].

Increasing the strength of magnetic field applied parallel to the c-axis further induces multiple AFM phases [phase A, B, and C in Fig. 1.8(b)] and a critical field around $B_c = 4.3$ T is observed that fully suppresses T_N [22] (Note that the parameter B used in [22] is intended to be the applied magnetic field H). Phase A has been shown to be an incommensurate partial AFM phase by neutron scattering studies, while phases B and C are canted AFM phases. The term *partial* AFM stresses the neutron and NMR results, that indicate one-third of the Ce moments do not order. Phases B and C show hysteresis in the electrical resistivity. Near the putative QCP at $B_c = 4.3$ T, an unkonwn phase D is inferred from shoulders observed in the temperature dependence of $d\rho/dB$ and ac susceptibility $\chi_{ac}(B)$. Phase E is a paramagnetic phase with a large negative magnetoresistance. The temperature dependence of the electrical resistivity below 0.3 K at all fields below 14 T exhibits a T^n behaviour with an anomalous exponent of $n > 2$. This has been attributed to AFM magnon excitations [22]. Above $B = 5$ T, a broad peak is observed in specific heat that shifts to higher temperature with increasing field. The behaviour of this peak can be understood by considering the electronic Schottky contribution, and in particular the Zeeman splitting of the ground state CEF doublet [53].

11
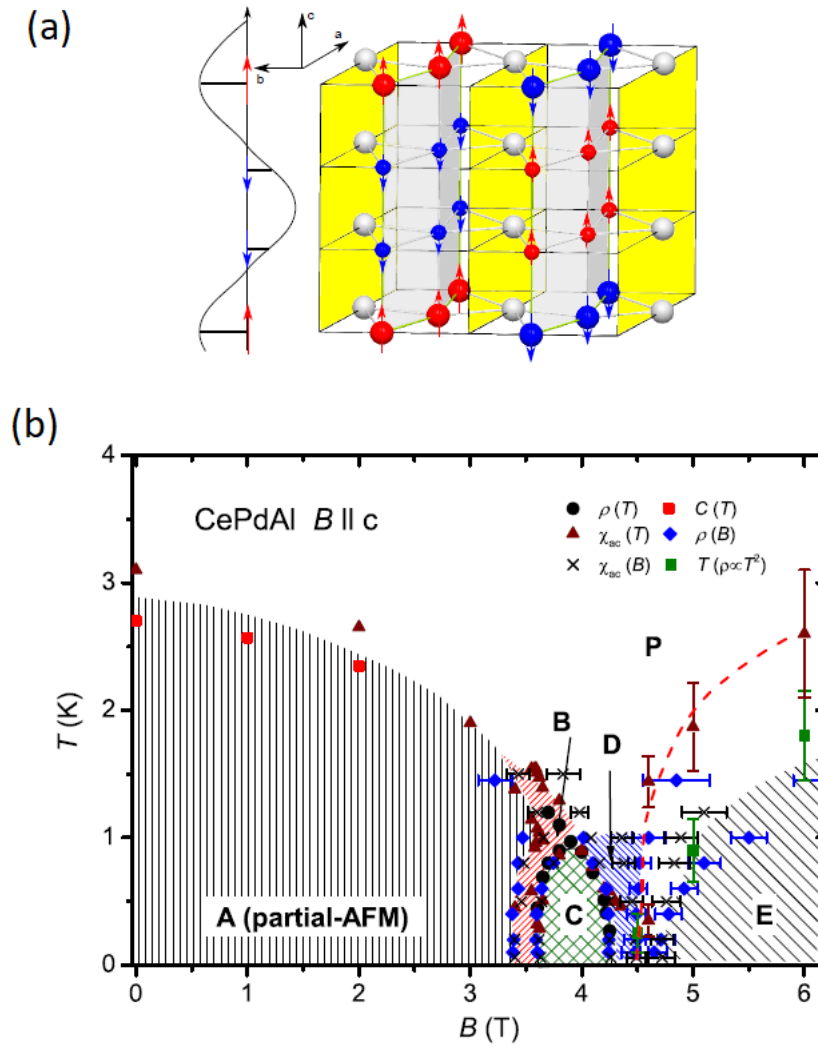
Figure 1.8: (a) Magnetic structure of CePdAl in zero-field proposed in [49]. The illustration is taken from [48]. The white spheres represent fluctuating Ce^{3+} spins. (b) The temperature-magnetic field phase diagram of CePdAl, taken from [22].

1.5.3 CePtPb

An earlier study of a single crystal of CePtPb by Movshovich *et al.* [54] demonstrated it to be a heavy-fermion compound with an AFM ground state. A fit of the temperature dependence of the inverse susceptibility [Fig. 1.9(a)] to the Curie-Weiss law above 150 K yields a Curie-Weiss temperature $\theta_{CW} = -40$ K and a Curie constant $C = 0.85$ emu/mol K. The corresponding effective moment $\mu_{eff} = 2.59$ μ_B/Ce is close to the free Ce^{3+} value, suggesting the ground state is magnetic. Below 150 K, a large magnetic anisotropy develops and increases to $\chi_{ab}/\chi_c = 11$ at 2 K. From ac magnetic susceptibility measurements [Fig. 1.9(b)], the ground state was confirmed to be AFM with a Néel temperature $T_N = 0.9$ K in ambient pressure. Under an applied pressure $P < 17$ kbar, the value of T_N increases approximately at a rate of 20 mK/kbar. The magnetic field dependence of the magnetization at 2.3 K [Fig. 1.9(c) and (d)] indicates that the *ab*-plane is the magnetic easy plane, with M_{ab} approaching saturation above 5 T and reaching a value of 1.05 μ_B/Ce at $B = 18$ T. On the other hand, M_c continues to grow markedly at 18 T, where it has a value of 0.35 μ_B/Ce. Note again the use of B rather than H for the applied magnetic field.

The overall behaviour of the electrical resistivity between 50 mK and 300 K suggests that the system is metallic in nature. A broad feature in the temperature dependence of $\rho(T)$ is observed around 5 K [Fig. 1.10(a)], which may be a signature of the Kondo effect or some short-range AFM correlations. A kink in $\rho(T)$ was also observed around 0.9 K [Fig. 1.10(b)] signifying the AFM transition. Between 50 mK and 0.7 K, $\rho(T)$ follows a T^2 dependence Fig. [1.10(b)], which is indicative of Fermi liquid behaviour.

The magnetic contribution to the specific heat of CePtPb, $C_m(T)$, is approximated by subtracting the specific heat of LaPtPb [Fig. 1.11(a)], which is a non-magnetic analogue that doesn't have magnetic $4f$-moments. A large Sommerfeld coefficient $\gamma = 300$ mJ/mol K^2 estimated [Fig. 1.11 inset] between 0.2 and 0.7 K from a linear fit of the C/T versus T^2 data, indicates heavy-fermion behaviour. The magnetic entropy, $S_m \equiv \int_0^T C_m/T dT$, below 20 K [Fig. 1.11(b)] shows saturating behaviour near $S_m = R \ln 2$, suggesting a doublet ground state. At T_N, only $0.4 R \ln 2$ of the magnetic entropy is recovered, possibly due to magnetic frustration or the Kondo effect.
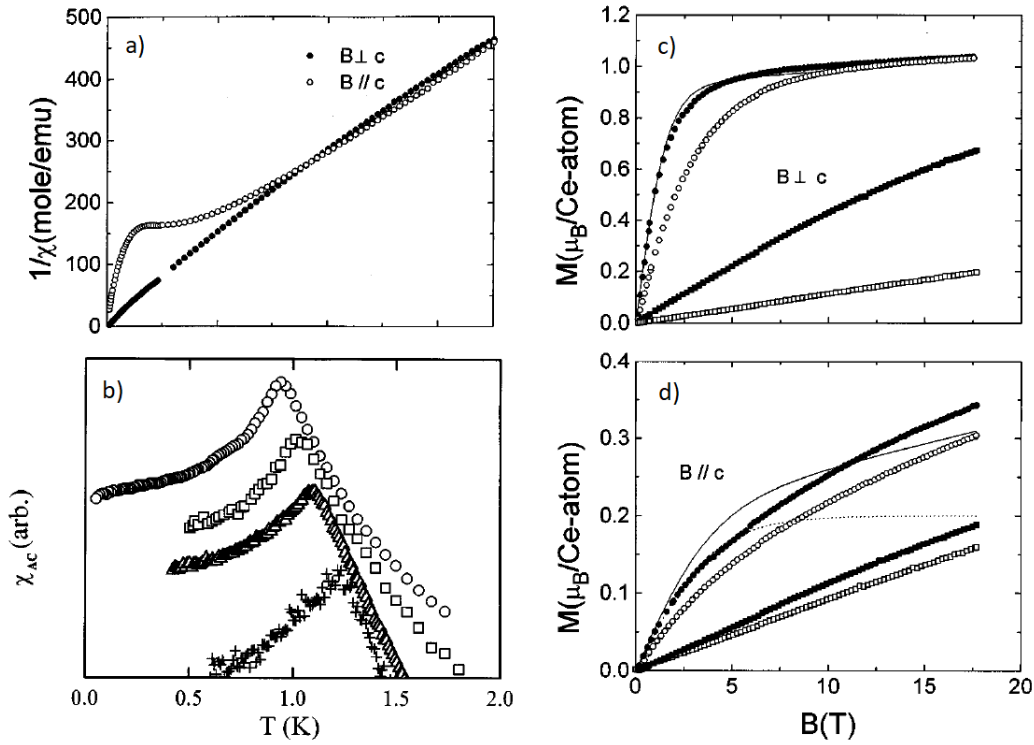
Figure 1.9: Previous magnetic susceptibility and magnetization study of CePtPb by [54]. (a) Temperature dependence of the inverse magnetic susceptibility for a magnetic field of 1 kOe applied parallel and perpendicular to the c-axis. (b) Temperature dependence of the ac magnetic susceptibility for different values of applied pressure. The peak indicative of the AFM transition shifts to higher temperature with increasing applied pressure between 0 and 17 kbar. (c) and (d) show the magnetic field dependence of the magnetization for fields perpendicular and parallel the c-axis at 2.3 K (solid circles), 4 K (open circles), 20 K (solid squares) and 100 K (open squares).
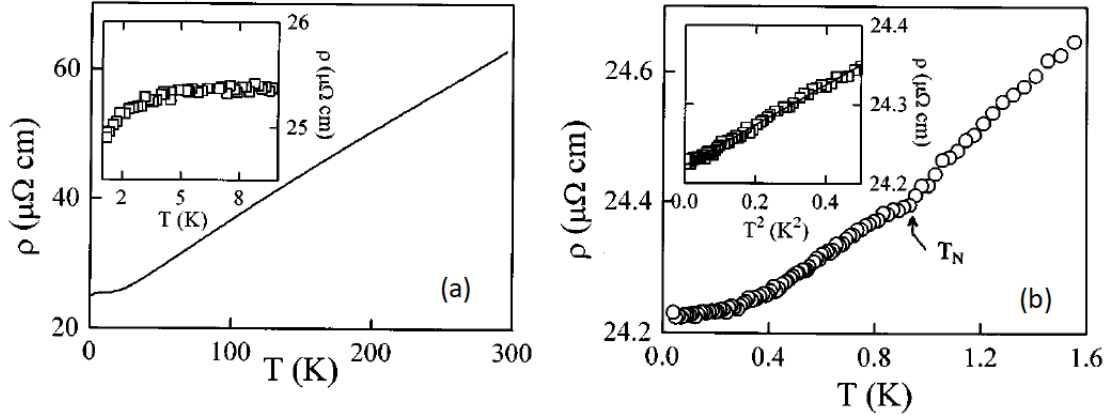
Figure 1.10: Previous zero-field measurements of the temperature dependence of the electrical resistivity of CePtPb [54]. (a) Temperature dependence of the resistivity between 50 mK and 300 K. Inset shows a blow up of the broad feature around 5 K. (b)Low temperature behavior of $\rho(T)$. The kink near 0.9 K is associated with an AFM transition. Inset shows the T^2 dependence of $\rho(T)$ below 0.7 K.
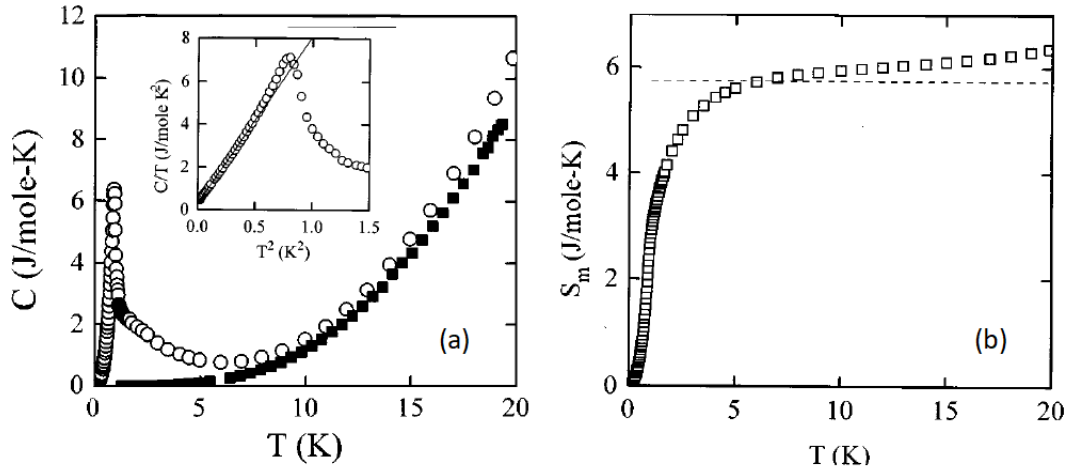
Figure 1.11: Previous zero-field specific heat study of CePtPb [54]. (a) Temperature dependence of the specific heat of CePtPb (open circles) and LaPtPb (closed squares). Inset shows a linear fit of C/T versus T^2 between 0.2 and 0.7 K. The slope of the fit provides an estimate of the Sommerfeld coefficient γ. (b) Temperature dependence of the magnetic entropy, showing a saturating behaviour near the value $S_{\mathrm{m}} = R \ln 2$ (dotted line) below 20 K.

Chapter 2

Experimental Methods

2.1 Sample Preparation

Single crystals of LaPtPb and CePtPb were grown out of Pb-rich solutions. The constituent elements with molar ratios of 4:4:92 (La:Pt:Pb) and 8:8:84 (Ce:Pt:Pb) for LaPtPb and CePtPb, respectively, were placed in an Al_2O_3 crucible sealed in a quartz ampoule. The crucibles were cushioned by quartz wool on either side to absorb spillage and to prevent cracking of the crucibles during the centrifuge process. The tubes were pumped and back-filled with argon gas at one fifth of atmospheric pressure.

The growth temperature profiles for the two compounds in a conventional radiation oven are shown in Fig. 2.1. For both compounds, the ovens were heated up quickly to 1180°C and left for 3 hours to thoroughly melt the elements in the crucibles before cooling slowly to maximize the growth process. The initial molar ratio of the elements, the number of heating and cooling steps, and their associated rates are set by the binary phase diagrams between the molar ratio of two elements and the temperature limit of the oven. For this experiment, the binary phase diagrams considered between all pairs of elements were obtained from [55].

The compounds were slowly cooled down to 600°C before being taken out of the oven and placed in a centrifuge to remove excess Pb flux in the crucibles. They were placed in hydrogen peroxide solutions for ten minutes to remove excess lead on the surface and then characterized by Laue and X-ray diffraction.

2.2 Sample Characterization

2.2.1 X-ray and Laue diffraction

Powder X-ray diffraction for CePtPb and LaPtPb were performed in a Rigaku MiniFlex diffractometer at room temperature with Cu K_α radiation to confirm the crystal structures and to determine the lattice parameters and the existence of any impurity phases. The facets of the as-grown single crystals are clearly visible in Fig. 2.1. The crystallographic c-axis is determined by Laue diffraction to be the needle axis.
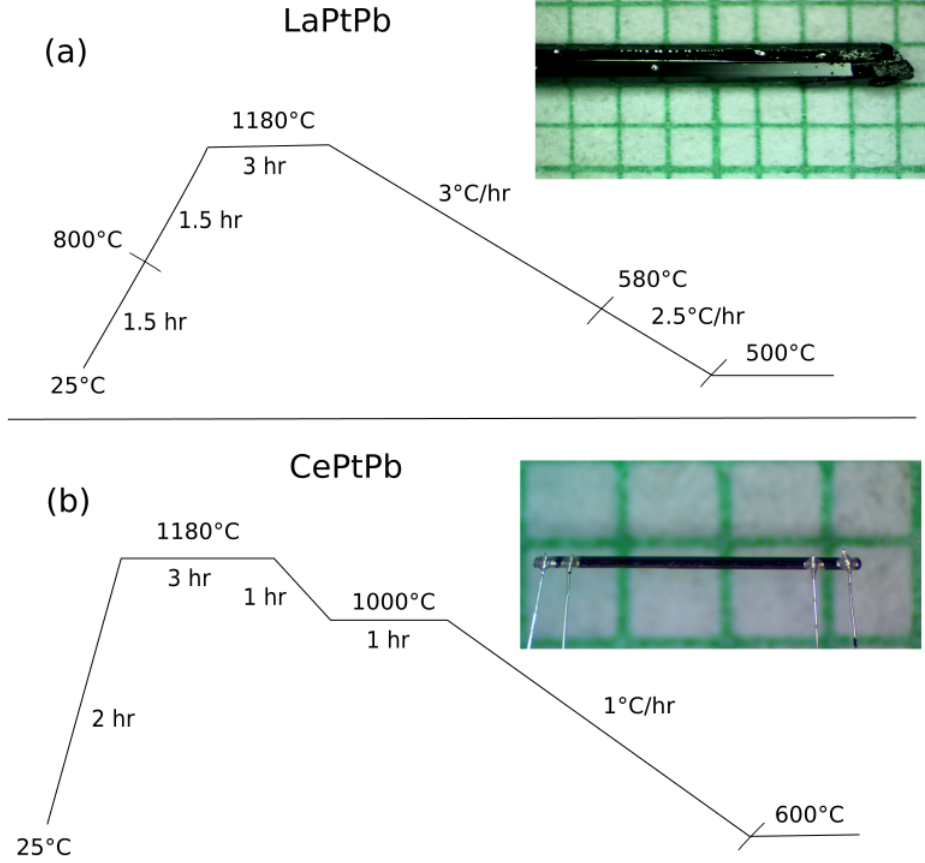
Figure 2.1: Flux growth timeline for (a) LaPtPb and (b) CePtPb with images of the single crystals shown on milimeter grid paper. The image for CePtPb also includes the silver epoxy and Pt leads that were used in the resistivity measurements.

2.2.2 Electrical resistivity measurement

The electrical resistivity of CePtPb was measured in a Quantum Design Physical Property Measurement System (PPMS) with a ^{3}He option in the temperature range of 0.4 to 300 K and applied magnetic field up to 90 kOe. A standard four probe method was used in which four Pt leads with a radius of ~ 50 μm were attached to the needle-shape sample with Epotek H20E silver epoxy. The epoxy was then cured at 120°C for 30 minutes on a hot plate. The sample was mounted onto a sample stage with Apiezon N grease, which provided a good thermal contact. The transverse magnetoresistance was measured with an ac current ($f = 16$ Hz) with the configuration $I \perp H$, $I \parallel c$, and $H \parallel ab$. The measured resistance R was converted to resistivity $\rho \equiv RA/l$, where A and l are the cross-sectional area and length between the two voltage leads of the sample, respectively.

2.2.3 Specific heat measurement

The specific heat of CePtPb and LaPtPb were also measured in the PPMS that was used for measuring the electrical resistivity, over similar temperature and field ranges (0.4 to 300 K with $H \leq 90$ kOe). The measurement was done using the relaxation method [56, 57] with the applied field in the ab-plane.

2.2.4 Magnetization measurement

The dc magnetization M of CePtPb and LaPtPb were measured in a Quantum Design Magnetic Property Measurement System (MPMS), which allows for measurements in the temperature range 1.8 to 300 K and an applied magnetic field $H \leq 70$ kOe. The samples were mounted between drinking straws by inserting one straw into another and sandwiching the samples in between them.

2.3 Muon Spin Relaxation (μSR)

The acronym μSR stands for Muon Spin Relaxation, Rotation, or Resonance, depending on the experimental configuration. The μSR methods utilized here for experiments on CePtPb probe the magnetism in the bulk via implantation of an ensemble of nearly 100% spin-polarized positive muons (μ^+). Unlike X-ray and neutron diffraction, there is no scattering of the μ^+ by the sample. The μSR method measures the time evolution of the muon-spin polarization $\mathbf{P}(t)$, which is governed by the local magnetic field $\mathbf{B}_{\text{loc}}$ at the μ^+ site. In general, $\mathbf{B}_{\text{loc}}$ is the vector sum of dipolar and hyperfine fields, and any external magnetic fields that may be applied.

The μSR experiments were performed using the M15 and M20D surface μ^+ beams at TRIUMF (Vancouver, Canada). The μ^+ in these beams have a kinetic energy of 4.12 MeV that results in a mean stopping range in the sample of ~140 mg/cm^2. In other words, to stop the μ^+ in a 140 mg sample, the cross-sectional area must be less than 1 cm^2. The implanted μ^+ quickly thermalizes and loses its kinetic energy within ~ 10 ps, which preserves the nearly 100% spin-polarization. In CePtPb, the implanted μ^+ comes to a rest at an interstitial site corresponding to a minimum in the electrostatic potential of the crystal lattice. The stability of the μ^+ site depends on the depth of the local electrostatic potential well and the thermal energy of the μ^+.

2.3.1 Muon decay

The μ^+ is an unstable particle with a mean lifetime of $\tau_\mu \sim 2.2$ μs. It decays via the weak interaction into a positron (e$^+$) according to

$$\mu^+ \rightarrow \text{e}^+ + \nu_\text{e} + \bar{\nu}_\mu, \tag{2.1}$$

where ν_e and $\bar{\nu}_\mu$ are the electron neutrino and muon antineutrino, respectively. Due to parity violation of the μ^+ decay, the decay e^+ has an angular probability distribution $W(E, \theta)$ given by

$$W(E, \theta) = 1 + a_0(E) \cos \theta, \tag{2.2}$$

where θ is the angle between the e^+ trajectory and the μ^+ spin direction, and a_0 is the initial asymmetry. The value of a_0 depends strongly on the kinetic energy E of the decay
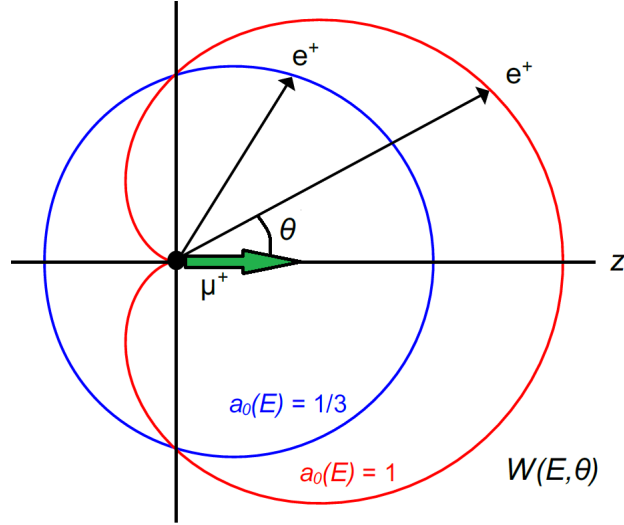
Figure 2.2: Angular probability distribution of e^+ emission for $a_0 = 1/3$ and 1. The green arrow indicates the μ^+ spin direction at the time of the decay and θ is the angle between the e^+ trajectory and the μ^+ spin direction.

e^+, which ranges from $E_{\min} = 0$ MeV to $E_{\max} = 52.3$ MeV. For a particular value of E, the value of a_0 is given by

$$a_0(\epsilon) = (2\epsilon - 1)/(3 - 2\epsilon), \tag{2.3}$$

where $\epsilon = E/E_{\max}$. The initial asymmetry a_0 varies monotonically from -1/3 for $\epsilon = 0$ to 1 for $\epsilon = 1$. However, the energy average of a_0 is 1/3, when all positron energies are considered with equal probability. Figure 2.2 shows $W(E, \theta)$ for $a_0 = 1/3$ and $a_0 = 1$. The z-axis in this figure is along the muon spin direction. The angular distribution function $W(E, \theta)$ is highly asymmetric for $a_0 = 1$, in which case no positrons of energy $E_{\max}$ are emitted antiparallel to the muon spin. For $a_0 = 1/3$, there is a non-zero probability of the e^+ being emitted in the antiparallel direction, however, the e^+ is still preferentially emitted in the same direction as the muon spin.

In the μSR experiment, the emitted e^+ is determined by the positron scintillator detectors that are placed around the sample environment. Given that the scintillator detectors do not differentiate the kinetic energy of the decay e^+, the maximum experimental value of a_0 is 1/3. However, the experimental value of a_0 is typically smaller due to a number

19

of experimental conditions, including the solid angle coverage of the detectors and their efficiency.

2.3.2 Experimental configuration

The μSR experiments were performed with zero-field (ZF) and longitudinal-field (LF) setups. The experimental arrangement of the LF setup for CePtPb is schematically shown in Fig. 2.3. The ZF setup is identical to the LF setup, except there is no applied field $\mathbf{B}_{\text{ext}}$. The initial muon-spin polarization $\mathbf{P}(0)$ was antiparallel to the μ^+ beam momentum. The beam axis is labeled as the z-axis in Fig. 2.3. The external magnetic field $\mathbf{B}_{\text{ext}}$ in the LF experiments was applied parallel to $\mathbf{P}(0)$. A thin muon scintillator detector was placed upstream of the sample to detect the arrival time of the μ^+ that is implanted in the sample. A "backward" positron scintillator detector was placed between the muon detector and the sample. The backward positron detector has a circular hole that allows the μ^+ to pass through to the sample. A "forward" positron detector was placed on the opposite side of the sample along the z-axis.
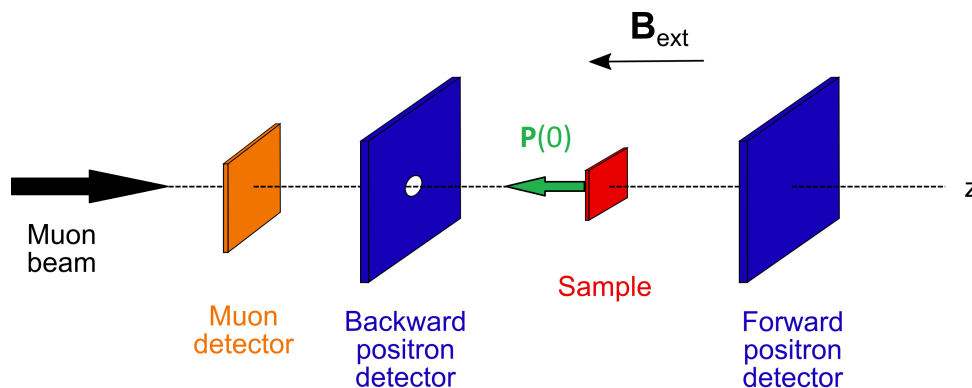
Figure 2.3: Schematic of the configuration used for the μSR experiments on CePtPb. The external magnetic field $\mathbf{B}_{\text{ext}}$ was applied in the LF-μSR experiments.

In both setups, a time-differential μSR method and a continuous muon beam were utilized. At time $t = 0$, the μ^+ passes through the muon detector, which triggers the start of an electronic clock. This instant is also considered to be the time the μ^+ comes to rest in the sample, because the time it takes for the μ^+ to travel from the muon detector to the sample is negligible. As time progresses, other μ^+ that pass through the muon detector are electronically excluded until the first decay e^+ is detected by either the forward or the backward positron detector. The electronic clock is stopped at time t when the first decay e^+ is detected. After accumulating several million μ^+ decay events, a time-differential histogram is constructed for each positron detector, which are related to the time evolution of the μ^+

spin polarization $P_z(t)$ as follows

$$N_F(t) = N_{0,F}e^{-t/\tau_\mu}[1 + a_0 P_z(t)] + B_F, \tag{2.4}$$

$$N_B(t) = N_{0,B}e^{-t/\tau_\mu}[1 - a_0 P_z(t)] + B_B, \tag{2.5}$$

where $N_{0,F}$ and $N_{0,B}$ are the normalization constants for the positron counts at $t = 0$, and B_F and B_B are time-independent backgrounds that arise from uncorrelated decay events (i.e., the time correlation between the μ^+ and its decay e^+ is lost). The time-independent background contribution is determined from the raw counts before $t = 0$ and subtracted from $N_F(t)$ and $N_B(t)$. The asymmetry spectrum $A(t)$ is then defined as

$$A(t) \equiv \frac{[N_F(t) - B_F] - [N_B(t) - B_B]}{[N_F(t) - B_F] + [N_B(t) - B_B]}. \tag{2.6}$$

In the ideal scenario where the forward and backward detectors are identical, have the same efficiency, and are placed exactly opposite to each other with the same solid angle coverage of the sample, $A(t)$ reduces to

$$A(t) = a_0 P_z(t). \tag{2.7}$$

Hence the asymmetry spectrum $A(t)$ directly reflects the time evolution of $P_z(t)$, which in turn contains information on the local magnetic fields at the muon site.

2.3.3 Muon polarization function

The time evolution of the muon-spin polarization in the z-direction of the μ^+ ensemble subject to a static, uniform local magnetic field ($\mathbf{B}_{loc}$) oriented at an angle θ with respect to the initial muon-spin polarization $\mathbf{P}(0) = P_z(0)\hat{z}$ is given by

$$P_z(t) = \cos^2\theta + \sin^2\theta\cos(2\pi\nu_\mu t), \tag{2.8}$$

where $\nu_\mu = \gamma_\mu/(2\pi)|\mathbf{B}_{loc}|$ is the μ^+ spin precession frequency and $\gamma_\mu/(2\pi) = 135.5$ MHz/T is the gyromagnetic ratio of the μ^+.

In general, the time evolution of the muon-spin polarization is calculated by averaging $P_z(t)$ over the local magnetic field distribution $n(\mathbf{B}_{loc}) = n(B_{loc,x})n(B_{loc,y})n(B_{loc,z})$ sensed by the μ^+ ensemble, where $B_{loc,i}$ ($i = x, y, z$) are the Cartesian components of $\mathbf{B}_{loc}$. The expression for $P_z(t)$ is then given by the volume integral over the local-field space

$$P_z(t) = \iiint n(\mathbf{B}_{loc})\left[\cos^2\theta + \sin^2\theta\cos(2\pi\nu_\mu t)\right]dB_{loc,x}dB_{loc,y}dB_{loc,z}. \tag{2.9}$$

Randomly-oriented static magnetic fields

In a single crystal of CePtPb, the nuclei of the atoms can be treated as a dense system of randomly-oriented magnetic dipole moments that are static on the μSR time scale. In this case, the field distribution for each component of the local magnetic fields is well approximated by a Gaussian distribution

$$n_{\mathrm{G}}(B_{\mathrm{loc,i}}) = \frac{\gamma_\mu}{\sqrt{2\pi\Delta_{\mathrm{G}}^2}}\exp\left(-\frac{\gamma_\mu^2 B_{\mathrm{loc,i}}^2}{2\Delta_{\mathrm{G}}^2}\right), \qquad (i = x, y, z), \tag{2.10}$$

where $\Delta_{\mathrm{G}}/\gamma_\mu$ is the field-distribution width. Substituting Eq. (2.10) into Eq. (2.9) and solving for the integral, one obtains what is known as the static Gaussian Kubo-Toyabe function [58]

$$P_{\mathrm{GKT}}(t) = \frac{1}{3} + \frac{2}{3}(1 - \Delta_{\mathrm{G}}^2 t^2)\exp\left(-\frac{\Delta_{\mathrm{G}}^2 t^2}{2}\right). \tag{2.11}$$

Figure 2.4(a) shows $P_{\mathrm{GKT}}(t)$ for different values of Δ_{G}. The polarization $P_{\mathrm{GKT}}(t)$ is characterized by a Gaussian damping at early times and a recovery to $P_{\mathrm{GKT}}(t) = 1/3$ at late times. This muon-spin polarization function also applies to a dense system of electronic dipole moments that are randomly-oriented and static on the μSR time scale.
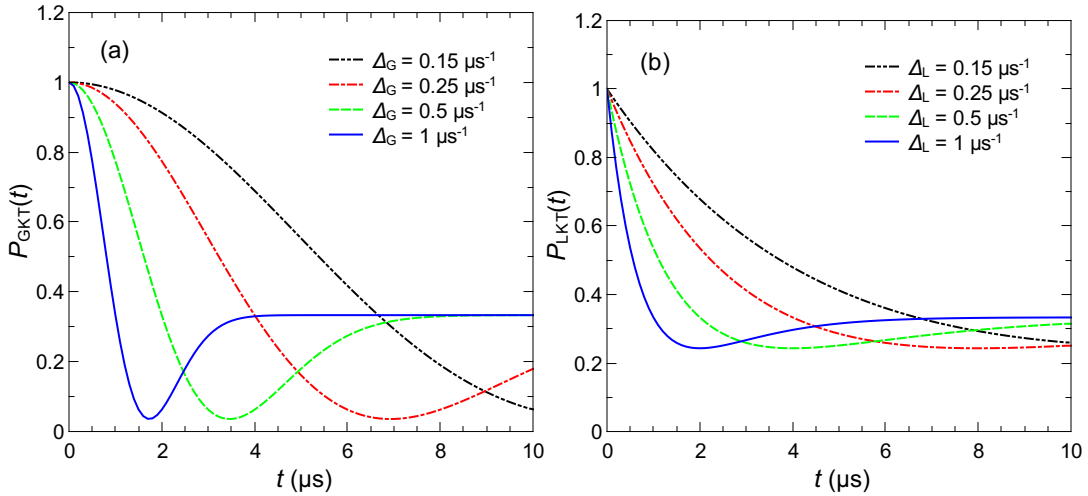
Figure 2.4: (a) Plots of the static Gaussian Kubo-Toyabe function $P_{\mathrm{GKT}}(t)$ given in Eq. (2.11) for different values of Δ_{G}. (b) Plots of the static Lorentzian Kubo-Toyabe function $P_{\mathrm{LKT}}(t)$ given in Eq. (2.13) for different values of Δ_{L}.

In contrast to a dense system of randomly-oriented magnetic dipole moments, a system with a dilute concentration of static magnetic moments has an approximately Lorentzian

distribution of field

$$n_{\mathrm{L}}(B_{\mathrm{loc,i}}) = \frac{\gamma_\mu}{\pi} \frac{\Delta_{\mathrm{L}}}{\Delta_{\mathrm{L}}^2 + \gamma_\mu^2 B_{\mathrm{loc,i}}^2}, \qquad (i = x, y, z), \qquad (2.12)$$

where $\Delta_{\mathrm{L}}/\gamma_\mu$ is the half-width at half-maximum (HWHM) of the field distribution. Calculating the integral in Eq. (2.9) with this Lorentzian field distribution yields the static ZF Lorentzian Kubo-Toyabe function [59]

$$P_{\mathrm{LKT}}(t) = \frac{1}{3} + \frac{2}{3}(1 - \Delta_{\mathrm{L}}t)\exp(-\Delta_{\mathrm{L}}t). \qquad (2.13)$$

Figure 2.4(b) shows $P_{\mathrm{LKT}}(t)$ for different values of Δ_{L}. $P_{\mathrm{LKT}}(t)$ is characterized by an exponential damping at early times and a shallower minimum than $P_{\mathrm{GKT}}(t)$. Similar to $P_{\mathrm{GKT}}(t)$, the function exhibits a recovery to the value $P_{\mathrm{LKT}}(t) = 1/3$ at late times. It is important to note that in a single crystal Eq. (2.11) and Eq. (2.13) are really approximations, as the isotropy assumed in the field distributions $n_{\mathrm{G}}(B_{\mathrm{loc,i}})$ and $n_{\mathrm{L}}(B_{\mathrm{loc,i}})$ are not valid. The long time recovery is not at $1/3$, but depends on the orientation of the crystal with respect to $\mathbf{P}(0)$. Nevertheless, the overall shape of the polarization function is similar.

Fluctuating magnetic fields

Fluctuations of the local magnetic field modify the muon-spin polarization function because the μ^+ senses time-varying fields over its lifetime. In the paramagnetic state of CePtPb, the effect of fluctuating electronic magnetic moments on the ZF-μSR signal is described by a dynamical muon-spin polarization function. For the purpose of this thesis, the discussion is restricted to the case of a fluctuating Gaussian distribution of local magnetic fields. In general, the dynamical muon-spin polarization function must be calculated numerically [60]. However, if the field fluctuation rate ν is sufficiently large compared to Δ_{G} ($\nu/\Delta_{\mathrm{G}} > 1$), the muon-spin polarization function is well approximated [61] by

$$P_{\mathrm{z}}(t) = \exp[-2(\Delta_{\mathrm{G}}^2/\nu^2)(e^{-\nu t} - 1 + \nu t)]. \qquad (2.14)$$

In the fast fluctuation limit, i.e. $\nu/\Delta_{\mathrm{G}} \gg 1$, $P_{\mathrm{z}}(t)$ approaches the exponential function [62]

$$P_{\mathrm{z}}(t) = e^{-\lambda t}, \qquad (2.15)$$

where $\lambda = 2\Delta_{\mathrm{G}}^2/\nu$.

A common method for measuring ν is to study the magnetic field response of the sample subjected to a longitudinal applied field $\mathbf{B}_{\mathrm{LF}} = B_{\mathrm{LF}}\hat{z}$. By replacing $B_{\mathrm{loc,z}}$ with $B_{\mathrm{loc,z}} + B_{\mathrm{LF}}$ and following the derivation presented in [61], the fast fluctuation limit for $P_{\mathrm{z}}(t)$ subjected to a longitudinal applied field is determined to also be an exponential decay function of the

form exp(-λt). However, the relaxation rate has a dependence on B_{LF} given by

$$
\begin{aligned}
\lambda(B_{\mathrm{LF}}) &= \frac{2\Delta_{\mathrm{G}}^2 \nu}{(\gamma_\mu B_{\mathrm{LF}})^2 + \nu^2} \\
&= \lambda(0)\frac{\nu^2}{(\gamma_\mu B_{\mathrm{LF}})^2 + \nu^2}.
\end{aligned}
\tag{2.16}
$$

This expression is sometimes referred to as the "Redfield" formula. When $B_{\mathrm{LF}} = 0$, one recovers the relaxation rate $\lambda(0) = 2\Delta_{\mathrm{G}}^2/\nu$ that is contained in Eq. (2.15). When a sufficiently large magnetic field is applied such that $\gamma_\mu B_{\mathrm{LF}}/\nu \gg 1$, the muon spin partially decouples from the internal magnetic field distribution. As shown in Fig. 2.5, this reduces the relaxation rate of $P_{\mathrm{z}}(t)$. In the $\gamma_\mu B_{\mathrm{LF}}/\nu = \infty$ limit, the muon spin fully decouples, sensing only the longitudinal field $\mathbf{B}_{\mathrm{LF}}$ that is parallel to $\mathbf{P}(0)$. In this limit, $P_{\mathrm{z}}(t)$ does not evolve with time.
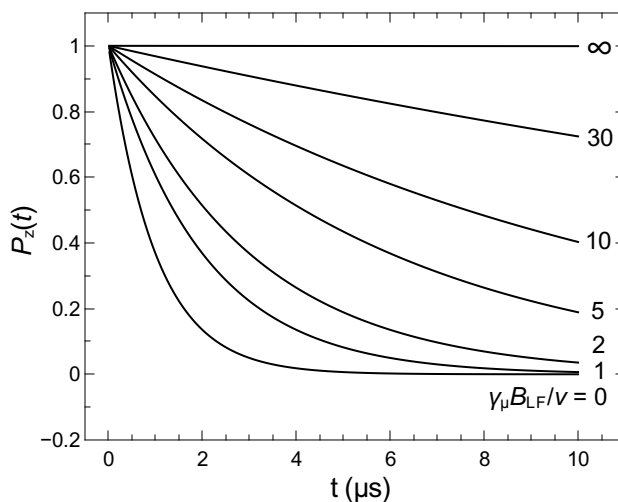
Figure 2.5: Plots of exp(-λt) with the relaxation rate $\lambda(H)$ given in Eq. (2.16), where ν is the fluctuation rate of the internal field distribution. The spectra are for different longitudinal applied magnetic fields B_{LF} and $\lambda(0) = 1$. When $\gamma_\mu B_{\mathrm{LF}}/\nu \gg 1$, the muon spin begins to decouple from the internal field distribution.

2.3.4 Experimental details

The experimental sample consisted of 21 single crystals of CePtPb that were glued onto a 12 mm × 16 mm high purity silver plate (99.999%) using GE varnish [Fig. 2.6]. The crystals were oriented along the *c*-axis and the normal direction of the silver plate was along the *z*-axis. This means that the initial muon-spin polarization $\mathbf{P}(0)$ was directed in the *ab*-plane of CePtPb. Given the magnetic field was applied in the direction of $\mathbf{P}(0)$ in the LF experiments, the applied field was also in the *ab*-plane. The temperature dependence of

the asymmetry spectrum $A(t)$ was measured from 25 mK to 3 K for ZF and longitudinal magnetic fields up to 9 kOe.

Figure 2.6: The oriented mosaic of CePtPb single crystals on a silver plate used in the μSR experiment.

Chapter 3

Data Analysis and Results

3.1 Laue and X-ray Diffraction

The crystallographic *c*-axis of CePtPb was confirmed using Laue diffraction with monochromatic X-rays projected along the needle axis [Fig. 3.1]. The diffraction spectrum agrees with the simulated spectrum for CePtPb along the (001) direction with a six-fold rotational symmetry. Powdered X-ray diffraction measurements [Fig. 3.2] on CePtPb and LaPtPb have

Table 3.1: The structural parameters of CePtPb and LaPtPb.

Compound	Space Group	a (Å)	c (Å)	Volume (Å^3)
CePtPb	P$\bar{6}$2m	7.730(2)	4.127(2)	213.6(1)
LaPtPb	P$\bar{6}$2m	7.774(3)	4.168(2)	218.2(2)

confirmed their space group to be P$\bar{6}$2m with the lattice constants and unit cell volumes listed in Table 3.1. The diffraction spectra shown in Fig. 3.2 reveals that these crystals have a single phase. The values of the structural parameters are consistent with the earlier reported values [54]. The uncertainties for the fitted lattice constants are estimated from allowing an angular offset to the fits to account for a possible false zero degree reading in 2θ due to limited machine accuracy.

3.2 Magnetization

The magnetic field dependence of the magnetization $M(H)$ for LaPtPb at $T = 2$ K is plotted in Fig. 3.3. The data are shown for a magnetic field H applied along the *c*-axis. When H is increased, the minor decrease in $M(H)$ is consistent with a diamagnetic response of the system.

The temperature dependence of the magnetic susceptibility $\chi(T) \equiv M/H$ for LaPtPb between 2 and 300 K is plotted in the inset of Fig. 3.3. The data are shown for a magnetic field $H = 70$ kOe applied along the *c*-axis. The susceptibility $\chi(T)$ decreases approximately linearly as the temperature decreases from 300 to 100 K, indicating a diamagnetic response
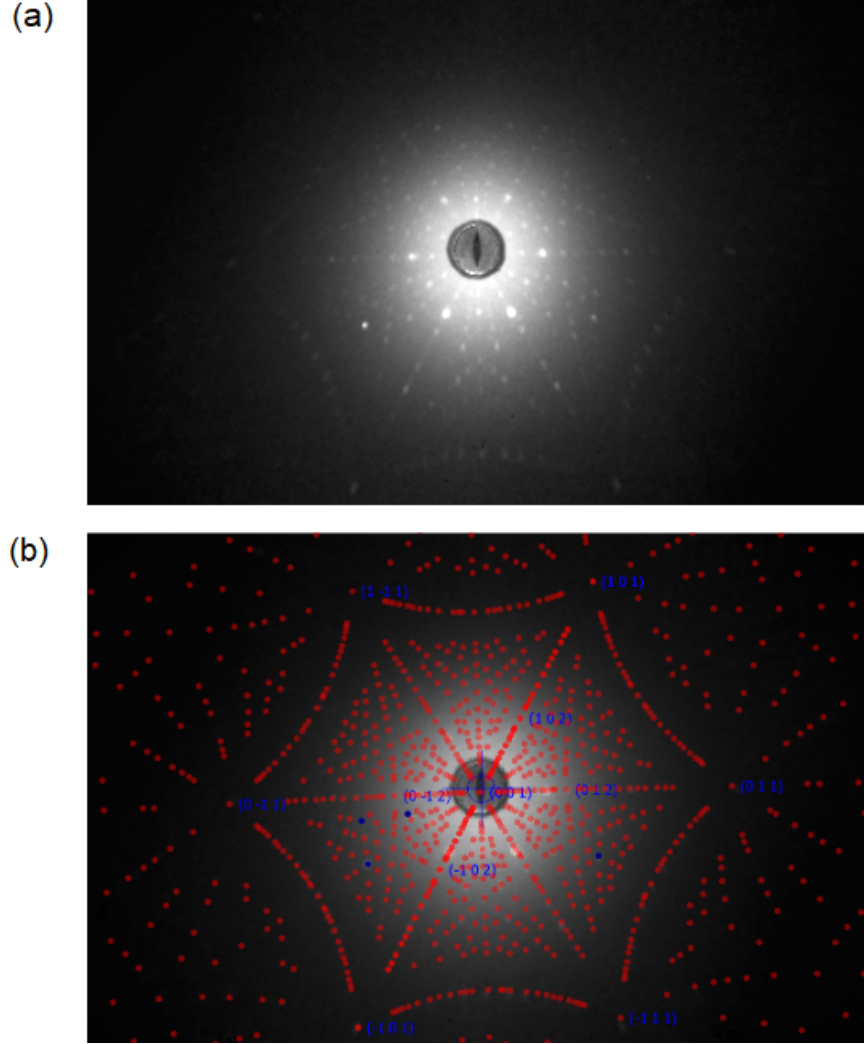
Figure 3.1: (a) Laue diffraction spectrum of CePtPb along the (001) direction. (b) Spectrum simulated from QLaue (red) overlaid on top of the diffraction spectrum.

in the system. When the temperature is lowered below 100 K, $\chi(T)$ exhibits an upturn, likely due to a dilute amount of paramagnetic impurities.

The magnetic field dependence of the magnetization for CePtPb at different temperatures is plotted in Fig. 3.4. The data are shown for a magnetic field H applied along the c-axis $[M_c(H)]$ and in the ab-plane $[M_{ab}(H)]$. At $T = 2$ K, $M_{ab}(H)$ saturates as the applied field H increases from 30 kOe to 70 kOe, whereas $M_c(H)$ continues to increase markedly with increasing field. At $T = 2$ K and $H = 70$ kOe, $M_{ab}(H)$ and $M_c(H)$ reach values of $\sim 1.1\ \mu_B/$Ce and $\sim 0.2\ \mu_B/$Ce, respectively. Overall, the measured magnetic susceptibility and magnetization are consistent with an earlier study [54].

The temperature dependence of the inverse magnetic susceptibility $1/\chi(T)$ for CePtPb between 1.8 and 300 K is shown in Fig. 3.5. The data are shown for a magnetic field $H =$
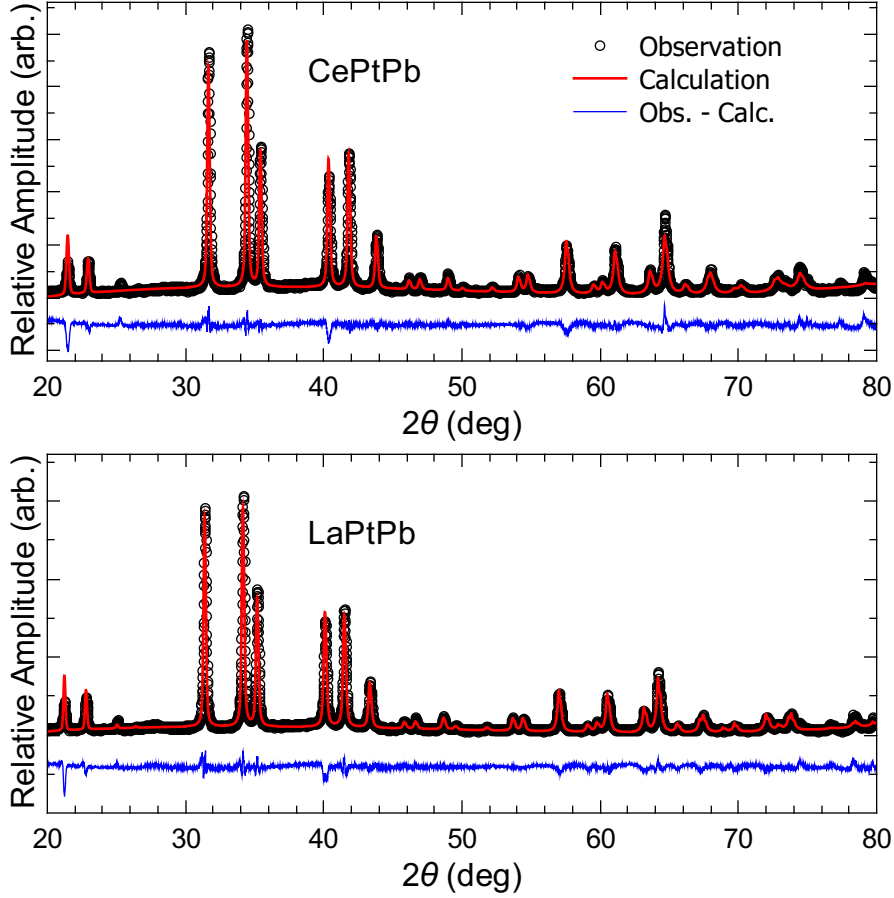
Figure 3.2: The observed powdered X-ray diffraction spectra of (a) CePtPb and (b) LaPtPb are shown by the black open circles. The red spectra are the calculated spectra using EdPCR [63]. The blue spectra are the difference between the measured and calculated diffraction spectra.

1 kOe applied along the c-axis $[1/\chi_c(T)]$ and in the ab-plane $[1/\chi_{ab}(T)]$. The polycrystalline average defined as $1/\chi_{avg}(T) \equiv 3/(2\chi_{ab} + \chi_c)$ is also plotted in Fig. 3.5. Below 150 K, a strong anisotropy develops between $1/\chi_{ab}(T)$ and $1/\chi_c(T)$. Furthermore, the ratio χ_{ab}/χ_c increases continuously as the temperature decreases, where χ_{ab}/χ_c has a value of ~ 17 at $T = 2$ K. The inverse c-axis magnetic susceptibility $1/\chi_c(T)$ shows a broad minimum around 70 K, a broad maximum around 30 K, and a rapid decrease below 30 K. Above 150 K, $1/\chi_{ab}(T)$, $1/\chi_c(T)$, and $1/\chi_{avg}(T)$ exhibit Curie-Weiss behaviour and are fit to the equation

$$\chi = \frac{C}{T - \theta_{CW}} + \chi_0, \tag{3.1}$$

where C is the Curie constant, θ_{CW} is the Curie-Weiss temperature, and χ_0 is a background contribution. The fitted values for each orientation of the applied field are summarized in
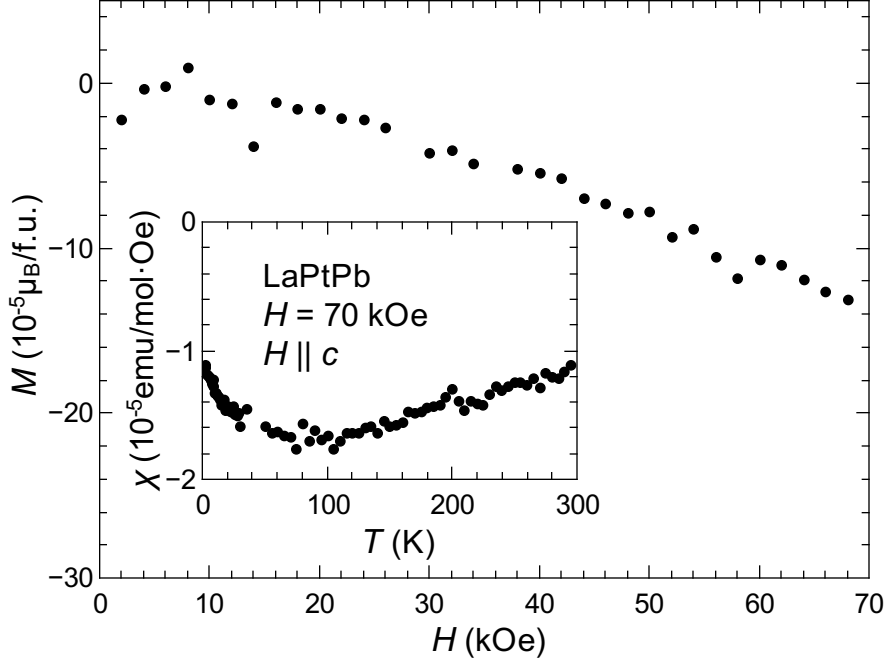
Figure 3.3: The *c*-axis magnetization of LaPtPb at 2 K. Inset: the *c*-axis magnetic susceptibility of LaPtPb at an applied magnetic field of $H = 70$ kOe. The upturn below 100 K is attributed to magnetic impurities.

Table 3.2. The effective moments calculated from C in all three cases are close to the free Ce^{3+} value of 2.54 μ_B, suggesting the Ce ions in the bulk of the sample have a $J = 5/2$ ground state. The fitted values of χ_0 are all in agreement with the magnetic susceptibility of isostructural single crystal LaPtPb, which doesn't have $4f$ electrons. The negative sign of θ_{CW} suggests an AFM ground state for the Ce ions, and the values of θ_{CW} are in good agreement with the earlier study [54]. The calculated frustration ratio from the polycrystalline averaged value of θ_{CW} is $f \approx -38/0.9 \approx -42$, suggesting that the system may be highly frustrated. However, this ratio may be influenced by the Kondo and CEF effects that are present in CePtPb.

Table 3.2: The fitted Curie constants (C), Curie-Weiss temperatures (θ_{CW}), background contribution to the magnetic susceptibility (χ_0), and the calculated effective moments (μ_{eff}) for CePtPb for a magnetic field $H = 1$ kOe applied in each crystallographic direction.

Field Orientation	C (emu/mol K)	θ_{CW} (K)	χ_0 (emu/mol Oe)	μ_{eff} (μ_B/Ce)
$H \parallel ab$	0.83	-33	-1.0×10^{-5}	2.58
$H \parallel c$	0.94	-51	-1.0×10^{-5}	2.75
Polycrystalline	0.86	-38	-1.0×10^{-5}	2.63
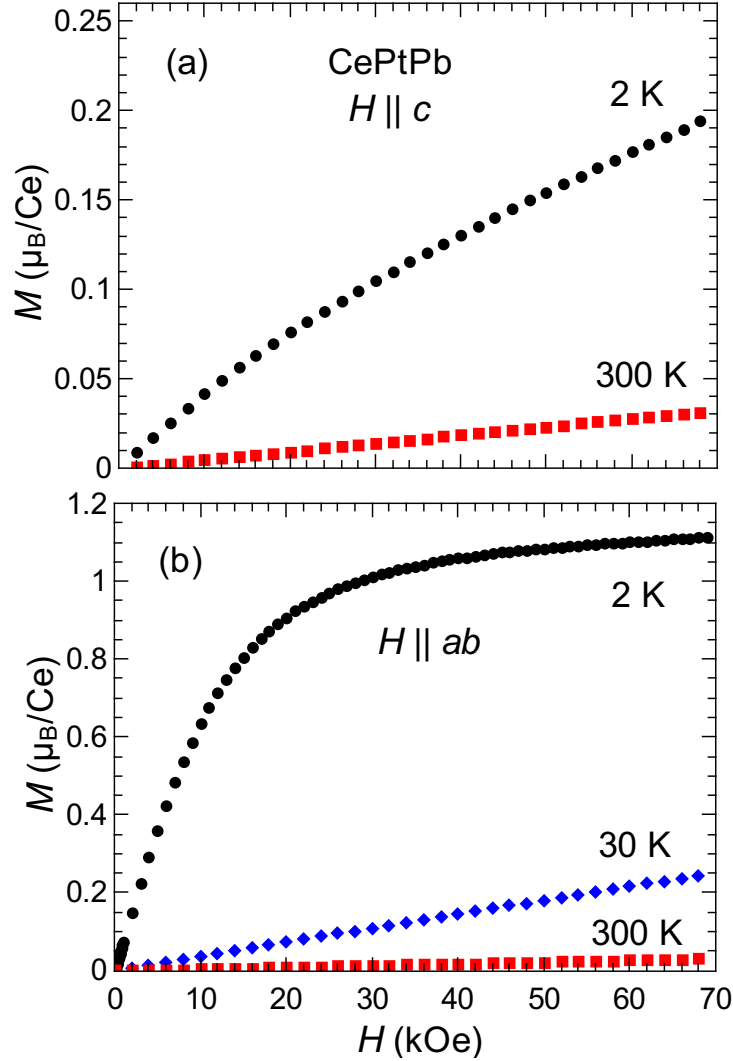
Figure 3.4: The magnetic field dependence of the magnetization for CePtPb for a magnetic field applied (a) along the c-axis and (b) in the ab-plane. The magnetization data are plotted at $T = 2$ K (circles), 30 K (diamonds), and 300 K (squares).

3.3 Electrical Resistivity

The temperature dependence of the electrical resistivity $\rho(T)$ for CePtPb measured in zero field is plotted in Fig. 3.6. The data are measured between 0.4 and 300 K. The overall behaviour of $\rho(T)$ is that of a metal. As the temperature is lowered from 300 to 150 K [Fig. 3.6(a)], $\rho(T)$ decreases linearly with decreasing temperature. From 150 to 20 K, $\rho(T)$ deviates from the linear temperature dependence and becomes slightly concaved down with decreasing temperature. From 10 to 5 K, $\rho(T)$ shows saturating behaviour [Fig. 3.6(a) inset]. Below approximately 5 K, $\rho(T)$ decreases rapidly. The origin of the behaviour near 5 K may be due to the Kondo effect or short range AFM correlations. The AFM order in CePtPb is
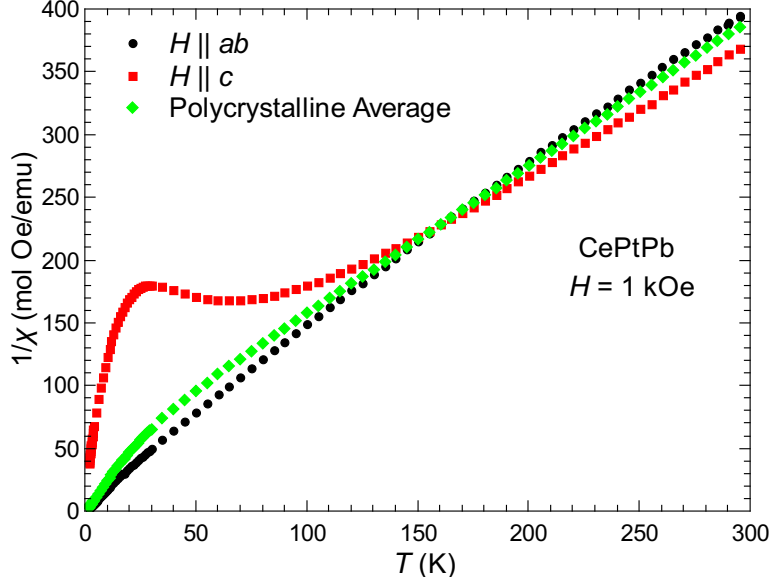
Figure 3.5: The temperature dependence of the inverse magnetic susceptibility for CePtPb between 1.8 and 300 K for a magnetic field of $H{=}1$ kOe applied along the c-axis (squares) and in the ab-plane (circles). The calculated polycrystalline average (diamonds) is also plotted.

observed as a change of slope at $T_N \approx 0.9$ K [Fig. 3.6(b)]. The shape of $\rho(T)$ around T_N is slightly different from the earlier study [54].

Between 0.4 and 0.9 K, a power-law analysis [Fig. 3.6(b) inset] of the form $\rho(T) = \rho_0 + AT^n$ yields $\rho_0 = 5.56$ $\mu\Omega$ cm, $A = 0.28$ $\mu\Omega/\mathrm{K}^{2.95}$, and $n = 2.95$. The fitted value of ρ_0 is four times smaller than that in the earlier study ($\rho_0 = 24.2$ $\mu\Omega$ cm), suggesting there are fewer impurities and crystal defects in the single crystal studied in this thesis. To further compare the quality of the single crystals, one can define a residual resistivity ratio (RRR) as $RRR = \rho(300\mathrm{K})/\rho(0.4\mathrm{K})$. A value of $RRR = 34.46/5.56 \approx 6.2$ is calculated, which is larger than $RRR = 60/24.25 \approx 2.5$ visually estimated from the temperature dependence of the electrical resistivity in Fig. 1.10(a) of [54]. Based on the lower ρ_0 and higher RRR, it is inferred that the quality of the single crystal CePtPb studied in this thesis is higher than that in the earlier study. The fitted value of $n \approx 3$ is also different from the earlier reported value of $n = 2$. A detailed analysis of this exponent as a function of applied magnetic field is given in Section 4.3.

Under an external magnetic field applied in the ab-plane [Fig. 3.7(a)], the change of slope associated with the AFM order in $\rho(T)$ is suppressed continuously to lower temperatures. Between 2 and 4 kOe, two changes of slope are observed, which are indicative of phase transitions. These phase transition points are further examined in Section 4.1. Hysteresis is observed between 1 and 3.5 kOe below T_N. As H increases from 10 kOe to 90 kOe [Fig. 3.7(b)], the reduced slope of $\rho(T)$ above 5 K shifts to higher temperatures, while $\rho(T)$ at
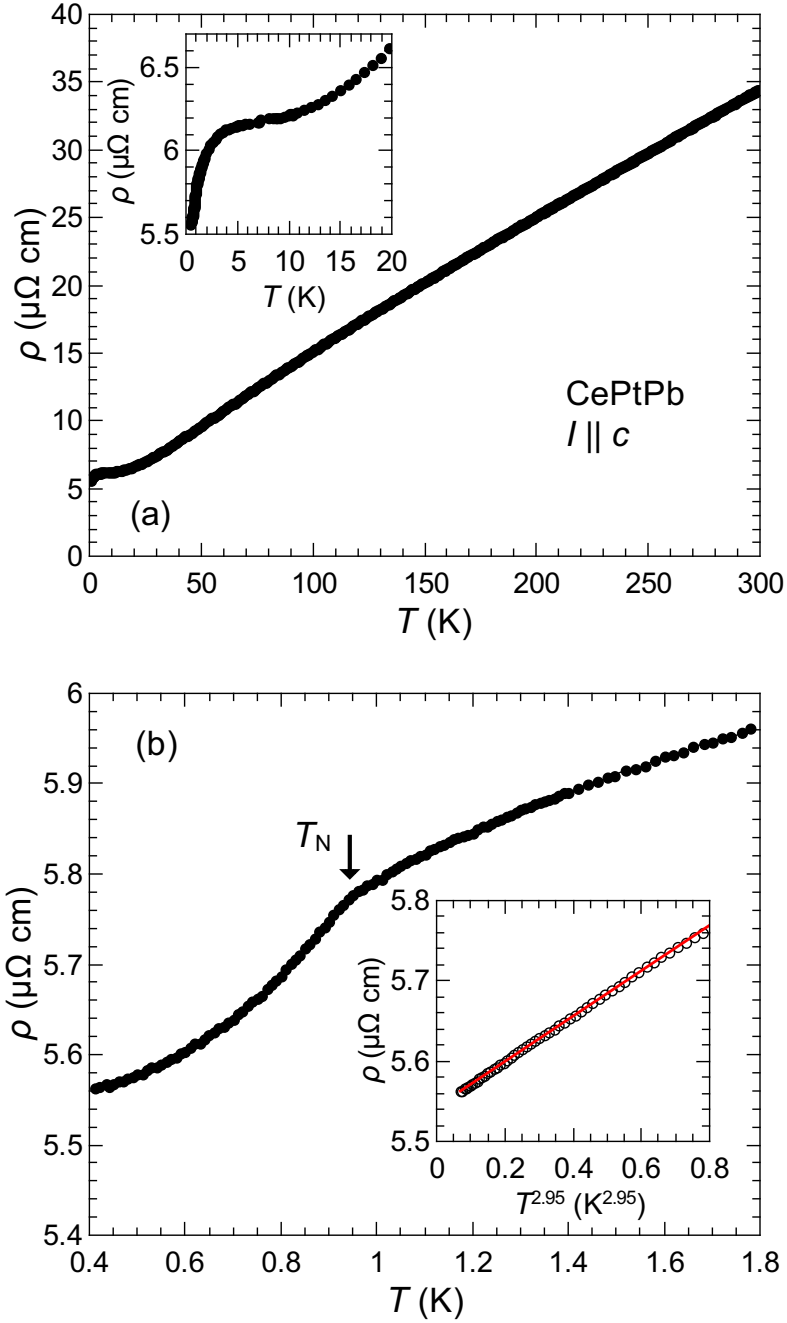
Figure 3.6: (a) The temperature dependence of the c-axis electrical resistivity $\rho(T)$ for CePtPb in zero field. The data are plotted for temperatures between 0.4 and 300 K. The inset shows a blow up of $\rho(T)$ below 20 K with the broad feature around 5 K. (b) A blow up of $\rho(T)$ below 1.8 K showing the signature of the AFM order at $T_N = 0.9$ K. The inset shows a linear fit to ρ versus $T^{2.95}$ below T_N.

low temperatures saturates; with the temperature-independent region extending to higher temperature as the field increases.
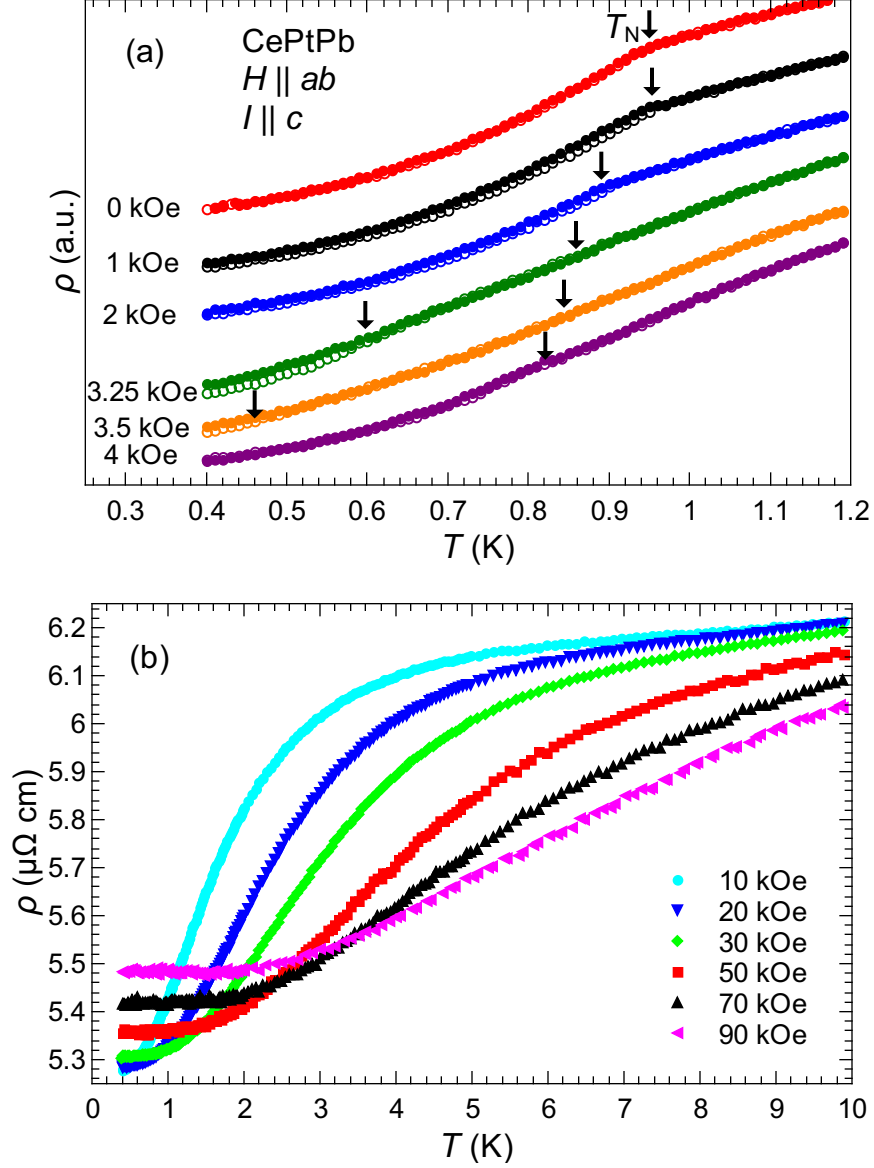
Figure 3.7: (a) The *c*-axis electrical resistivity for CePtPb measured as a function of increasing (open circles) and decreasing (closed circles) temperature in magnetic fields applied in the *ab*-plane. The arrows indicate the Néel temperatures. (b) The temperature dependence of the *c*-axis resistivity for CePtPb for different applied magnetic fields between 10 and 90 kOe. The $H = 90$ kOe data were taken while warming and the other data was taken while cooling.

Figure 3.8(a) shows the magnetic field dependence of the electrical resistivity $\rho(H)$ for CePtPb for magnetic fields $H \leq 10$ kOe applied in the *ab*-plane. Above T_{N}, $\rho(H)$ decreases gradually as H increases. When CePtPb is cooled below T_{N}, $\rho(H)$ exhibits multiple behaviours as a function of H. At $T = 0.4$ K, $\rho(H)$ appears to be constant with field between

33
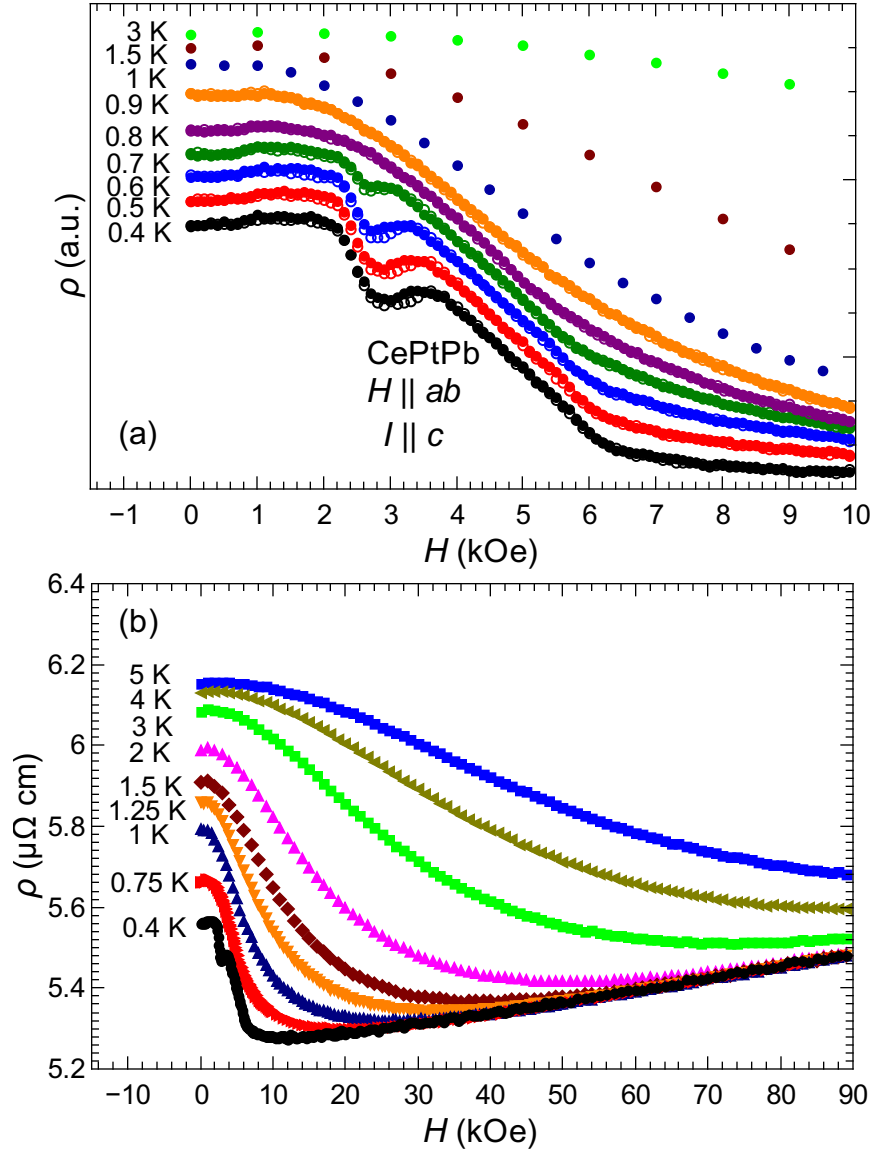
Figure 3.8: (a) The *c*-axis electrical resistivity measured as a function of increasing (open circles) and decreasing (closed circles) magnetic fields applied in the *ab*-plane at different temperatures. (b) The magnetic field dependence of the *c*-axis electrical resistivity for CePtPb for applied fields up to 90 kOe at different temperatures. The $T = 0.4, 0.75, 1.25, 1.8, 2,$ and 4 K data are taken while warming and the other data are taken while cooling.

0 and 0.8 kOe. Around 0.8 kOe, there is a slight increase in $\rho(H)$ as the field increases, followed by a rapid decrease around 2.2 kOe. A minimum is observed around 3 kOe, followed by a maximum near 3.6 kOe. Hysteresis is observed in the applied field range between 0.8 and 3.6 kOe. Around 6 kOe, a slope change is observed. As the temperature increases, the

feature around 0.8 K appears to be temperature independent while the observed minimum, maximum, and the slope change around 6 kOe in $\rho(H)$ gradually shift to lower values of H.

Figure 3.8(b) shows $\rho(H)$ for $H \leq 90$ kOe for different temperatures. At $H = 40$ kOe and $T = 5$ K, an inflection is observed in $\rho(H)$. As the temperature decreases, this inflection point shifts to lower values of H and persists below T_{N}. At $T = 0.4$ K, $\rho(H)$ exhibits a linear field dependence for applied fields approximately above 20 kOe and overlaps with the $\rho(H)$ data at other temperatures for sufficiently high applied fields. This may be related to the field-induced saturated paramagnetic state of the Ce-$4f$ spins. Futhermore, at a given applied field H, the temperatures where the different $\rho(H)$ measurements overlap with each other coincide with the temperatures where $\rho(T)$ saturates at that field [Fig. 3.7(b)]. Therefore, the low temperature saturation behaviour in $\rho(T)$ for the different applied fields is also attributed to this field-induced saturation effect.

3.4   Specific Heat

The temperature dependence of the specific heat $C_{\mathrm{p}}(T)$ for CePtPb and LaPtPb measured in zero field are plotted in Fig. 3.9(a). The measurements are made between 0.4 and 300 K. The overall behaviour of the specific heat for LaPtPb [denoted $C_{\mathrm{LaPtPb}}(T)$] is similar to that of simple metals such as copper [64, 65] and silver [64]. Between 1.8 and 25 K, $C_{\mathrm{LaPtPb}}(T)$ is well described by

$$C_{\mathrm{p}}(T) = \gamma T + \beta T^3, \tag{3.2}$$

which yields the Sommerfeld coefficient $\gamma = 3.9$ mJ/mol K^2 and $\beta = 1.0$ mJ/mol K^4. A Debye temperature $\Theta_{\mathrm{D}} \approx 180$ K for LaPtPb is estimated from the fitted value of β.

The behaviour of the specific heat for CePtPb [denoted $C_{\mathrm{CePtPb}}(T)$] above 10 K is similar to $C_{\mathrm{LaPtPb}}(T)$. At $T_{\mathrm{N}} \approx 0.9$ K, the signature of the AFM order for CePtPb is observed as a peak in $C_{\mathrm{CePtPb}}(T)$. The Sommerfeld coefficient of CePtPb [inset of Fig.3.9(a)] is estimated by a linear least-square fit to a plot of C_{p}/T versus T^2 between 0.16 and 0.4 K^2, which yields a value of $\gamma \approx 0$ mJ/mol K^2. An attempt to estimate the coefficient from the paramagnetic state is shown in the inset of Fig. 3.9(b). By using the data between $T^2 = 65$ and 500 K^2, a linear least-square fit yields a small value of $\gamma = 6$ mJ/mol K^2. These values are very different from the earlier reported value of $\gamma \approx 300$ mJ/mol K^2 [54].

Experimentally, the magnetic contribution to the specific heat of CePtPb may be approximated by

$$C_{\mathrm{m}}(T) \equiv C_{\mathrm{CePtPb}}(T) - C_{\mathrm{LaPtPb}}(T). \tag{3.3}$$

As seen in Fig. 3.9(b), $C_{\mathrm{m}}(T)$ has a sharp peak at T_{N} with a tail that extends to ~ 10 K and a broad peak centered around 100 K that is due to CEF effect. The solid curve in Fig.
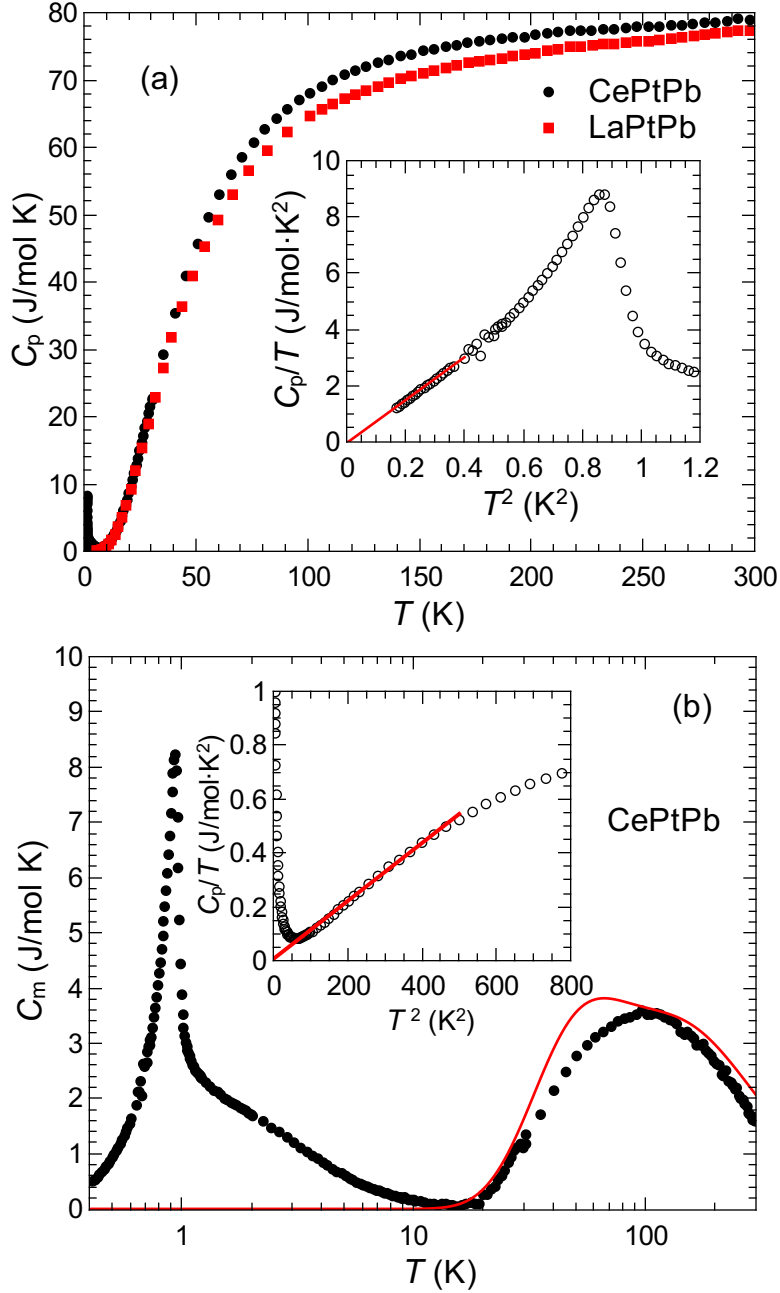
Figure 3.9: (a) The temperature dependence of the specific heat $C_p(T)$ for CePtPb and LaPtPb in zero field. The inset is a plot of C_p/T versus T^2 for CePtPb. The line is a linear fit between 0.16 and 0.4 K^2 extrapolated to zero temperature. (b) The magnetic contribution to the specific heat for CePtPb. The curve is a fit to the three-level Schottky anomaly model given in Eq. (3.4), which assumes each CEF energy level has a doublet degeneracy. The inset is a plot of C_p/T versus T^2 for CePtPb. The line is a linear fit between 65 and 500 K^2 extrapolated to zero temperature.
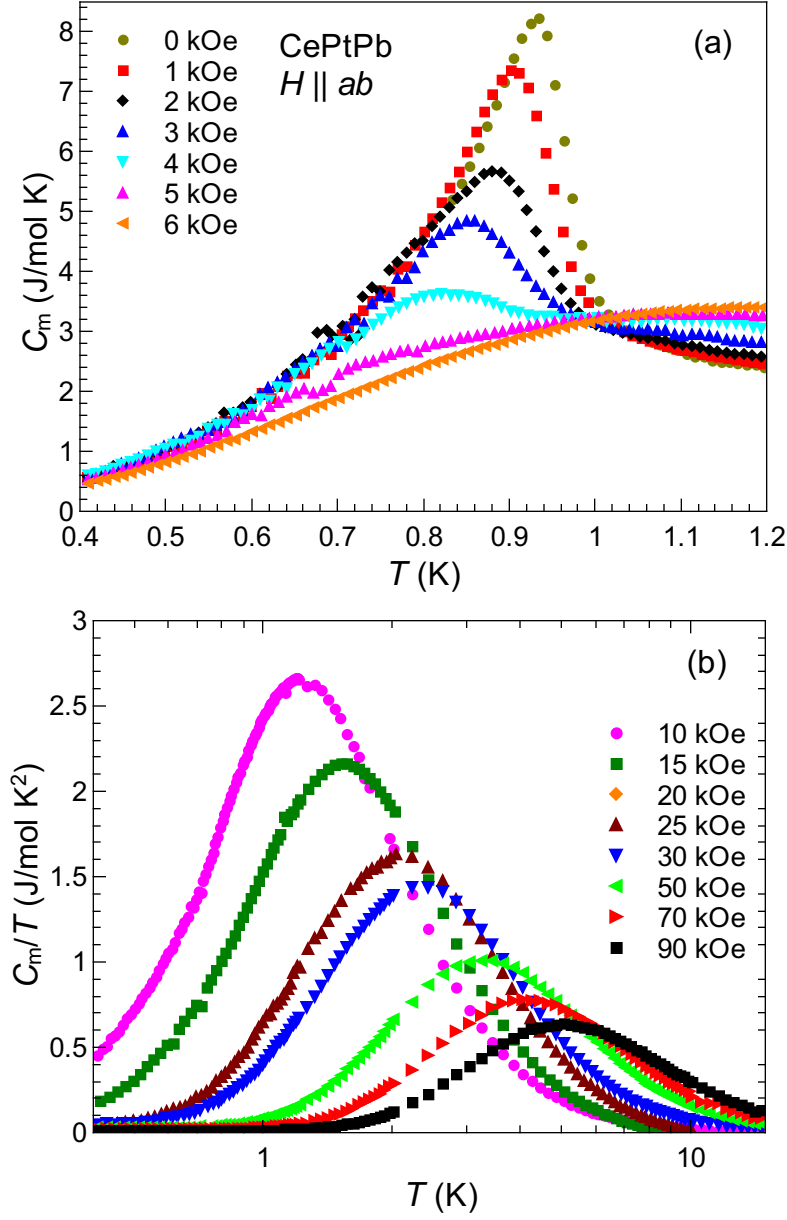
Figure 3.10: (a) The temperature dependence of the magnetic contribution to the specific heat $C_{\mathrm{m}}(T)$ of CePtPb for magnetic fields $H \leq 6$ kOe applied in the ab-plane. (b) A plot of C_{m}/T versus T for magnetic fields H between 10 and 90 kOe applied in the ab-plane.

3.9(b) is an attempt to fit this broad peak with a three-level Schottky anomaly given by

$$C_{\mathrm{Sch,three}}(T) = \frac{k_{\mathrm{B}}}{T^2 Z^2}\left[\Delta_1^2 g_0 g_1 e^{-\Delta_1/T} + \Delta_2^2 g_0 g_2 e^{-\Delta_2/T} + (\Delta_1-\Delta_2)^2 g_1 g_2 e^{-(\Delta_1+\Delta_2)/T}\right], \quad (3.4)$$

where k_{B} is the Boltzmann constant, $Z = g_0 \exp(-\beta E_0) + g_1 \exp(-\beta E_1) + g_2 \exp(-\beta E_2)$ is the partition function, $g_0 = g_1 = g_2 = 2$ are the degeneracies of the three energy levels, and

$k_B\Delta_i$ for $i = 1, 2$ are the energies of the excited levels. The formula assumes $\Delta_0 = 0$ K. The fit yields $\Delta_1 = 141$ K and $\Delta_2 = 489$ K.

For small magnetic fields $H \leq 6$ kOe applied in the ab-plane [Fig. 3.10(a)], the sharp peak at T_N in zero field broadens and shifts to lower values of temperature as the applied field increases. At $H = 10$ kOe [Fig. 3.10(b)], a peak is clearly observed around $T = 1.2$ K, which broadens and shifts to higher values of temperature as the magnetic field increases to $H = 90$ kOe.
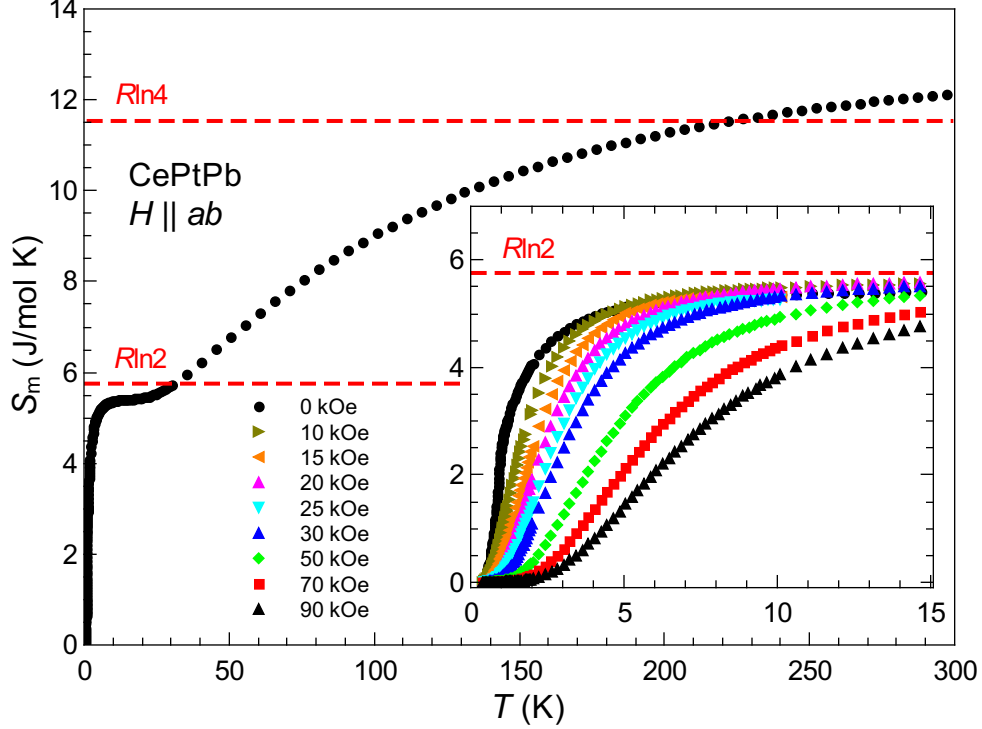
Figure 3.11: The temperature dependence of the magnetic entropy $S_m(T)$ for CePtPb in zero field. The inset shows $S_m(T)$ for different magnetic fields applied in the ab-plane for $T \leq 15$ K.

The magnetic entropy $S_m(T)$ for $T > 0.4$ K is defined as follows

$$S_m(T) = \int_{0.4}^{T} \frac{C_m(T)}{T} dT. \tag{3.5}$$

The temperature dependence of $S_m(T)$ for magnetic fields applied in the ab-plane are plotted in Fig. 3.11. In zero field, $S_m(T)$ increases rapidly as the temperature increases from 0.4 to 3 K. An inflection point is observed at T_N. Above 3 K, $S_m(T)$ appears to approach saturation near a value of $R \ln 2$ up to 15 K, suggesting a CEF doublet ground state. Above 25 K, $S_m(T)$ increases appreciably with temperature up to 300 K, reaching a value of $R \ln 4$ at 200 K without any sign of saturating to this value.

At T_N, a magnetic entropy of $0.4R\ln 2$ is recovered, consistent with the earlier study [54]. Moreover, the full value of the $R\ln 2$ entropy is not recovered until a temperature $T_S \approx 25T_N$. The high T_S/T_N ratio can have two possible origins. The first one is short-range magnetic or AFM correlations (e.g. magnetic frustration), which is observed even in simple antiferromagnets such as $NiCl_2$ [66]. The second possibility is Kondo screening of the Ce^{3+} ions by the conduction electrons. Under magnetic fields $H \geq 10$ kOe applied in the ab-plane, the behaviour of $S_m(T)$ associated with the ground state doublet broadens with the applied field and T_S is pushed to higher temperatures, consistent with a Zeeman splitting of the ground state doublet.
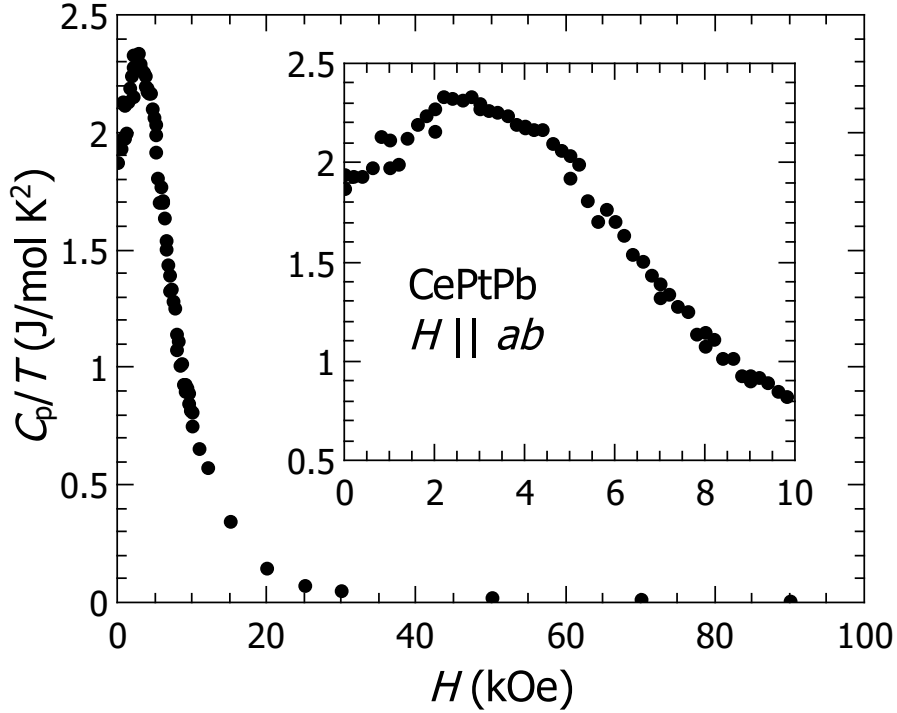
Figure 3.12: The magnetic field dependence of the specific heat $C_p(H)$ for CePtPb at $T = 0.5$ K. The data is plotted in terms of C_p/T versus H. The inset is a blow up of C_p/T for $H \leq 10$ kOe.

The magnetic field dependence of the specific heat $C_p(H)$ for CePtPb at $T = 0.5$ K for magnetic fields applied in the ab-plane is shown in Fig. 3.12. The data are plotted as C_p/T versus H. Despite the scatter in the data points, it is clear that $C_p(H)/T$ increases gradually from 1.94 J/mol K^2 at $H = 0$ kOe to 2.3 J/mol K^2 at $H = 2.5$ kOe. There appears to be a change of slope around 1 kOe. A broad maximum is observed around $H = 2.5$ kOe and $C_p(H)/T$ decreases quickly as H increases from 2.5 to 90 kOe, with an inflection point observed around $H = 6.5$ kOe.

39

3.5 μSR

The zero-field (ZF) asymmetry spectra $A(t)$ for CePtPb between 0.03 and 9 μs at various temperatures are plotted in Fig. 3.13. The first 30 ns of the spectra are potentially contaminated by μ^+ that missed the sample and triggered the positron detectors directly, and consequently has been removed. Above T_N, $A(t)$ decays slowly as a function of time. This is consistent with fast Ce-4f spin fluctuations in the paramagnetic state. In this regime, the asymmetry spectra are well described by a fit function of the form

$$A(t) = A_S e^{-\lambda t} P_{GKT}(t) + A_B, \tag{3.6}$$

where $P_{GKT}(t)$ is a temperature-independent static Gaussian Kubo-Toyabe function with a fitted relaxation rate $\Delta_G = 0.07~\mu s^{-1}$, and A_S and A_B are the sample and background contributions to the initial asymmetry a_0, respectively. The background component arises from μ^+ that did not stop in the CePtPb sample, but rather in the Ag backing plate and in parts of the cryostat. The static Gaussian Kubo-Toyabe function $P_{GKT}(t)$ accounts for the nuclear dipole moments in CePtPb, which are randomly oriented and static on the μSR time scale. The exponential relaxation function describes the contribution from the Ce-4f spins.
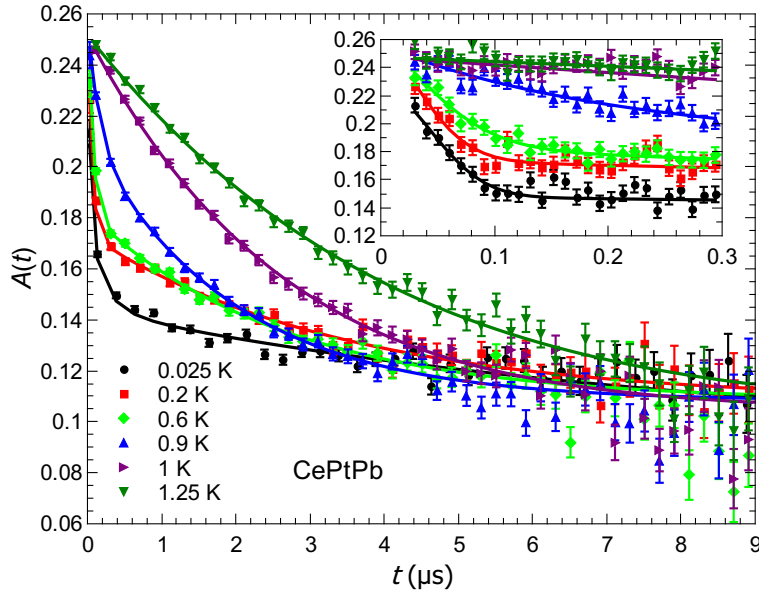
Figure 3.13: Representative ZF-μSR asymmetry spectra for CePtPb at various temperatures. The initial muon spin polarization $\mathbf{P}(0)$ was parallel to the ab-plane. Each data point shown is an average of 250 raw data points packed in a time bin $\Delta t = 97.7$ ns and the curves are fits to the raw data (see main text). The inset shows the spontaneous development of a rapid decrease in $A(t)$ at early time below T_N. Each data point shown is an average of 10 raw data points packed in a time bin $\Delta t = 3.9$ ns.

When CePtPb is cooled below T_N, a rapid decrease in $A(t)$ develops within the first 0.1 μs. The asymmetry spectra $A(t)$ for $T < T_N$ are well described by the following three-component fit function with two exponentially damped terms

$$A(t) = A_1 e^{-\lambda_1 t} + A_2 e^{-\lambda_2 t} + A_B, \tag{3.7}$$

where A_1 and A_2 are the asymmetry contributions from muons stopping in the sample, such that $A_S = A_1 + A_2$. The two exponential terms are associated with slow-relaxing and fast-relaxing components with corresponding exponential relaxation rates λ_1 and λ_2.
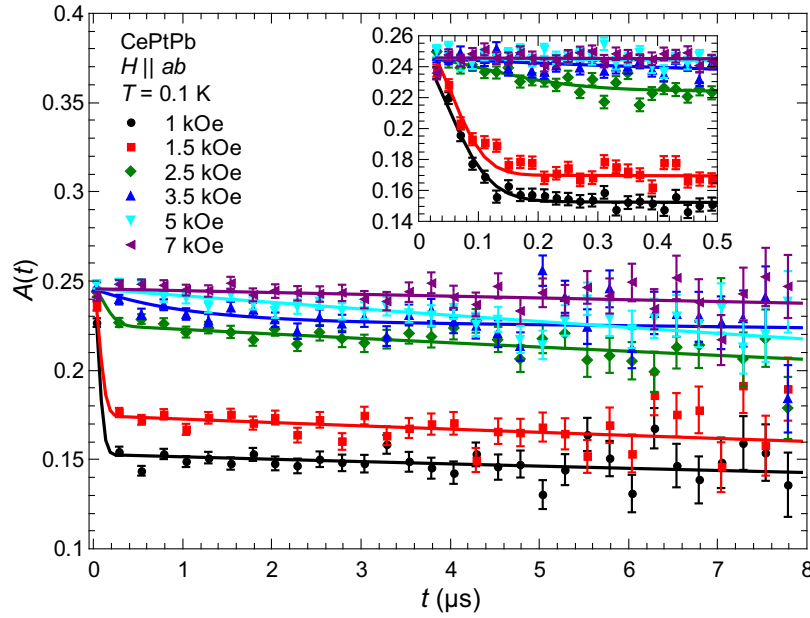
Figure 3.14: Representative LF-μSR asymmetry spectra for CePtPb at $T = 0.1$ K, for various applied magnetic fields. The initial muon spin polarization $\mathbf{P}(0)$ was parallel to the ab-plane. Each data point shown is an average of 250 raw data points packed in a time bin $\Delta t = 97.7$ ns and the curves are fits to the raw data (see main text). The inset is a blow up of $A(t)$ over the first 0.5 μs, where each data point shown is an average of 10 raw data points packed in a time bin $\Delta t = 3.9$ ns.

In a longitudinal magnetic field (LF) applied in the ab-plane [Fig. 3.14], the fast relaxing component of $A(t)$ at $T = 0.1$ K is suppressed continuously with the applied field. For an applied field $H \geq 3.5$ kOe, $A(t)$ at all temperatures is well described by a single exponential function of the form

$$A(t) = A_S e^{-\lambda t} + A_B. \tag{3.8}$$

Note that the first term does not include $P_{GKT}(t)$, as the applied field decouples the muon spin from the nuclear dipole fields, which are on the order of 1 G. The temperature depen-

dence of the fitting parameters in zero field and at different applied fields are shown in Figs. 3.15 and 3.16, respectively.
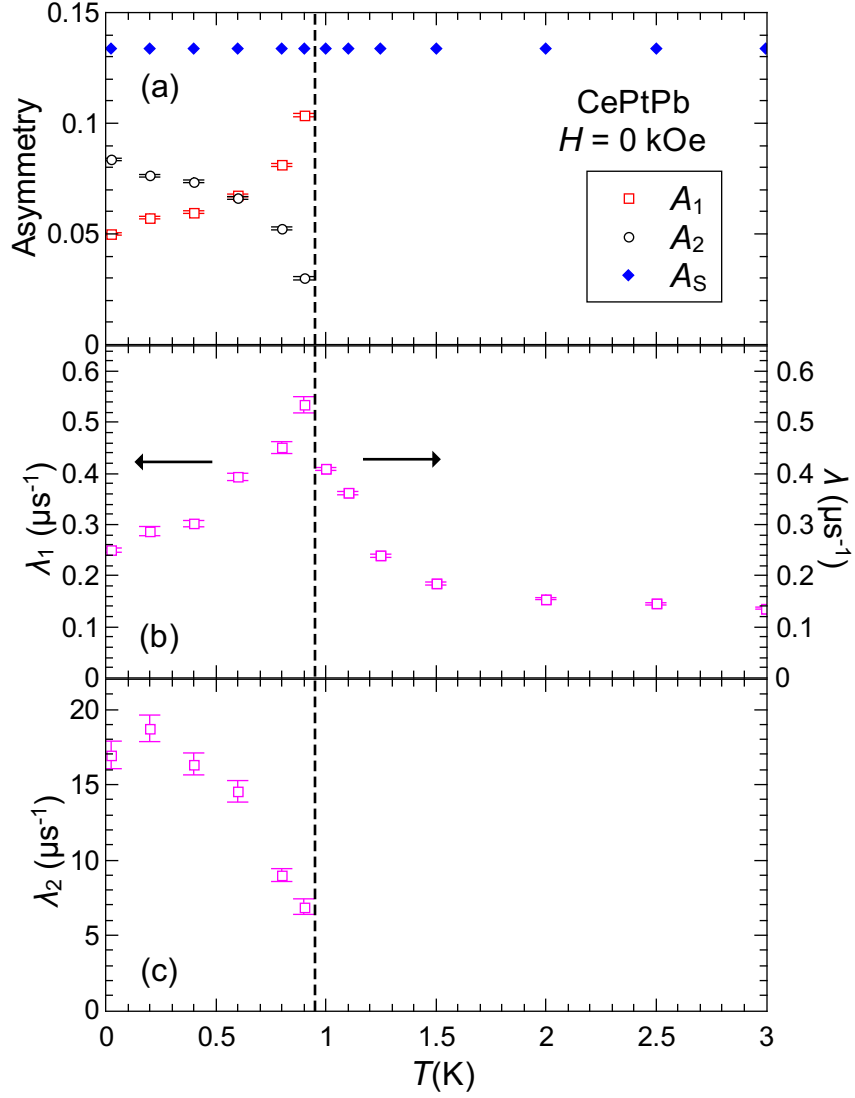
Figure 3.15: Temperature dependence of the ZF-μSR fit parameters for CePtPb. (a) Temperature dependence of the sample asymmetries A_1 and A_2 associated with the slow- and fast-relaxing exponential components of Eq. (3.7). The sample asymmetry A_S from Eq. (3.6) above T_N is also shown along with the temperature dependence of $A_S = A_1 + A_2$ above T_N. (b) and (c) show the fitted exponential relaxation rates associated with Eq. (3.6) and Eq. (3.7). The dashed vertical line indicates the Néel temperature T_N in zero field determined by the specific heat measurements.
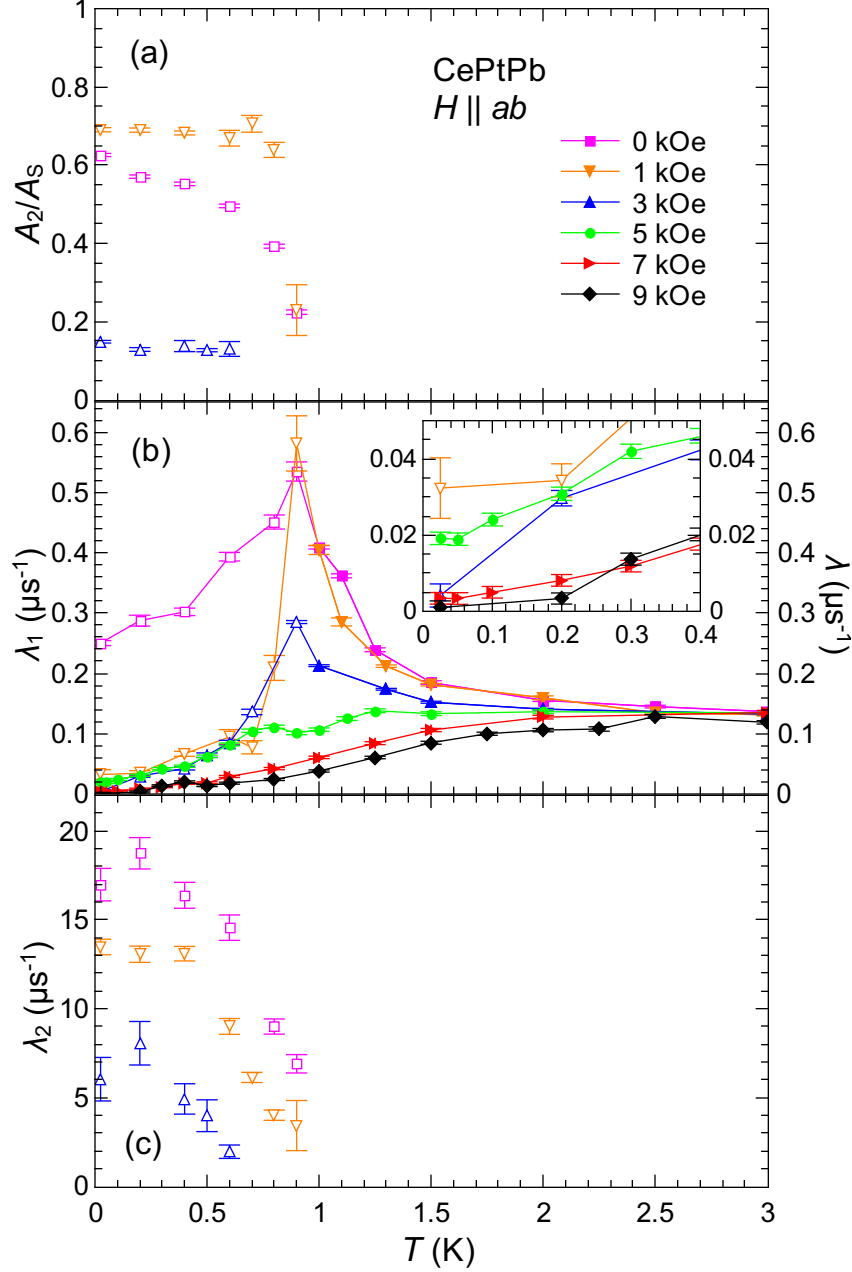
Figure 3.16: Temperature dependence of the ZF-μSR and LF-μSR fit parameters for CePtPb. (a) The normalized sample asymmetry A_2/A_S associated with the fast-relaxing exponential component of Eq. (3.7). (b) The exponential relaxation rates λ (closed symbols) for the sample signal from fits to Eq. (3.6) and Eq. (3.8) and the slow-exponential relaxation rate λ_1 (open symbols) from fits to Eq. (3.7). (c) The exponential relaxation rate λ_2 of the sample asymmetry associated with the fast-relaxing exponential component of Eq. (3.7).

Chapter 4

Discussion

4.1 Construction of T-H Phase Diagram

A temperature versus magnetic field (T-H) phase diagram for CePtPb can be constructed for external magnetic fields applied in the ab-plane from the anomalies observed in the data for $\rho(T, H)$ and $C_m(T, H)$. For $C_m(T, H)$, the feature associated with the AFM order in CePtPb is a peak at T_N in zero field [Fig. 3.10(a)], which shifts to lower values of temperature as the applied field is increased up to $H = 7$ kOe. At $H = 7$ kOe, a different peak is observed at $T \sim 1.2$ K, which shifts to higher values of temperature as the applied field is increased up to $H = 90$ kOe. Above 30 kOe, this peak becomes too broad to determine the temperature of the peak maximum. For $\rho(T, H)$, the features associated with the AFM order are indicated by peaks and kinks in the temperature and field derivatives of ρ, as shown in Figs. 4.1(a) and 4.1(b). The anomalies in $d\rho/dH$ at $T = 0.4$ K [Fig. 4.1(a)] evolve smoothly as the temperature is increased and disappear above T_N. On the other hand, the anomaly associated with the AFM order in $d\rho/dT$ [Fig. 4.2(b)] evolves smoothly to lower values of temperature as the applied field is increased to $H = 5.5$ kOe. Above this field, the anomaly disappears. Between 2 and 4 kOe, another anomaly is apparent at lower temperatures. For $H \geq 6$ kOe, a broad peak is observed above T_N and shifts to higher values of temperature as the applied field increases to $H = 90$ kOe. The anomalies in $C_m(T, H)$ and $\rho(T, H)$ are compiled in the temperature-versus-magnetic field phase diagram shown in Fig. 4.3.

Similar to CePdAl and YbAgGe, the constructed phase diagram for CePtPb shows multiple regions. The AFM transition temperature $T_N \approx 0.9$ K in zero field is continuously suppressed by field to $T = 0.4$ K at $H = 6.6$ kOe, with a linearly extrapolated critical applied field $H_c \approx 7$ kOe. Between 0.8 and 3.5 kOe, hysteresis is observed in $\rho(T, H)$. Without further knowledge from neutron diffraction measurements, the magnetic structure of each ordered region remains unclear.
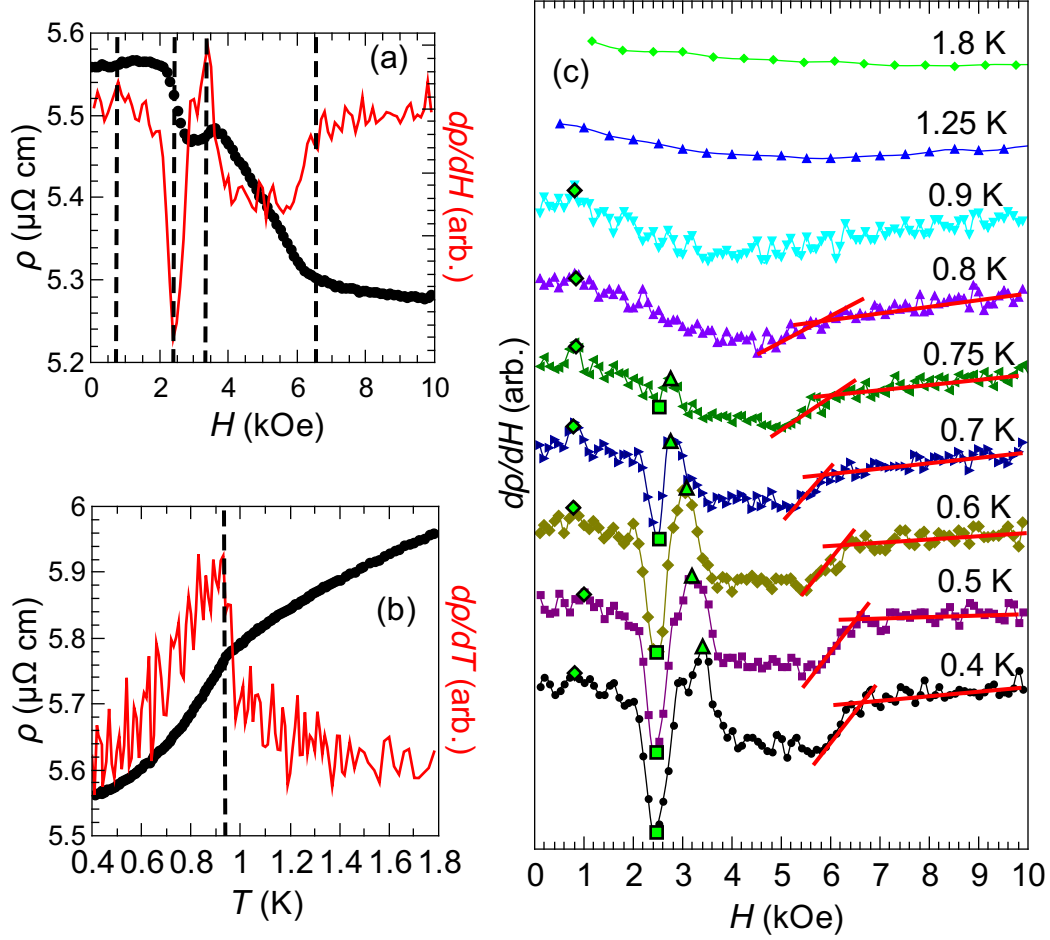
Figure 4.1: (a) The magnetic field dependence of the electrical resistivity $\rho(H)$ for CePtPb at $T = 0.4$ K plotted together with the derivative $d\rho/dH$. The data were measured as a function of increasing applied field. (b) The temperature dependence of the electrical resistivity $\rho(T)$ for CePtPb in zero field plotted together with the derivative $d\rho/dT$. The data were measured while warming. The vertical dashed lines in (a) and (b) indicate the phase transition points. (c) The magnetic field dependence of $d\rho/dH$ at different temperatures. The $\rho(H)$ data were for increasing applied field. The $d\rho/dH$ data points are connected by lines. The red lines are guides to the eye for the observed anomalies. The phase transition are indicated by the black edge diamonds, squares, and triangles, and are also indicated by the intercepts of the red lines.
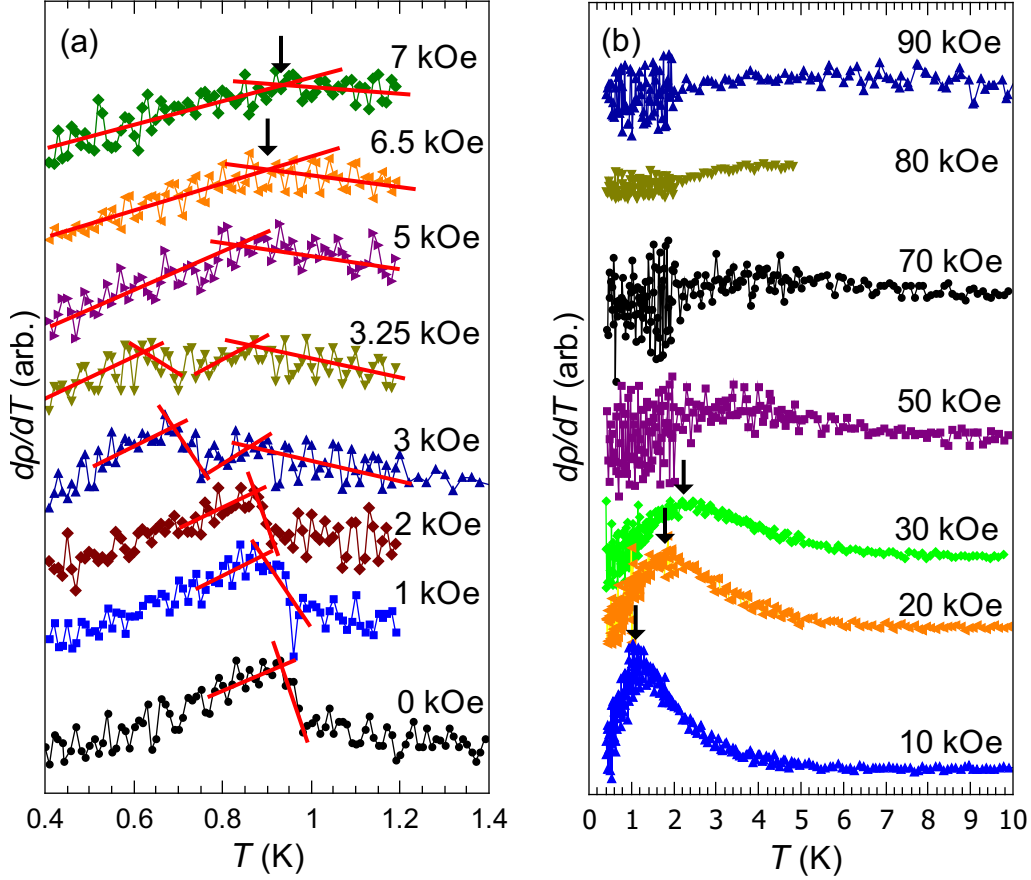
Figure 4.2: The temperature dependence of $d\rho/dT$ for (a) $H \leq 7$ kOe and (b) $H \geq 10$ kOe applied in the ab-plane. All of the $\rho(T)$ data in this figure, except the 80 and 90 kOe data, were measured while cooling. The data are connected by lines and the red lines are guides to the eye for the observed anomalies. The phase transitions occur at the intercept of the red lines for $H \leq 5$ kOe. For $H \geq 6.5$ kOe, a different anomaly is observed where the peak is indicated by the arrows.
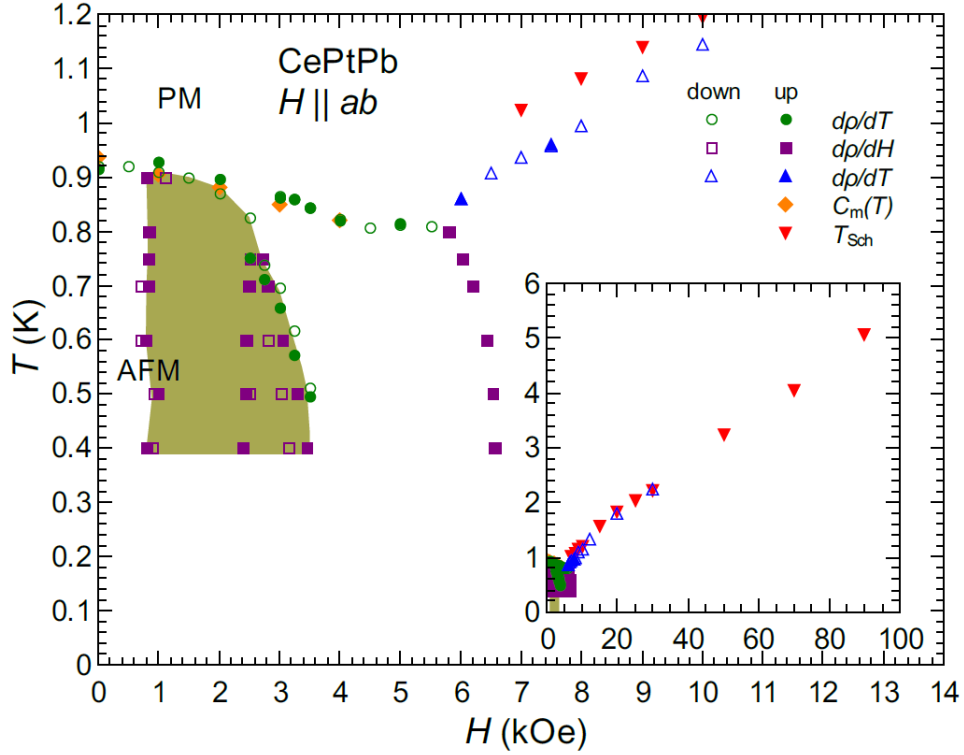
Figure 4.3: Temperature-versus-magnetic field phase diagram for CePtPb (with the magnetic field applied in the ab-plane) inferred from the $\rho(T, H)$ and $C_{\mathrm{m}}(T, H)$ measurements. The diamonds are the phase transitions observed in the temperature dependence of the magnetic specific heat. The nablas are the temperature of the maximum of the broad peak seen in the magnetic specific heat for $H \geq 7$ kOe, which is qualitatively described by an electronic Schottky anomaly. The circles and squares are phase transitions indicated in the temperature derivative and the field derivative of the electrical resistivity, respectively. The triangles are the anomaly observed in the field derivative of the resistivity for $H \geq 6$ kOe. The shaded region represents the part of the phase diagram where hysteresis is observed in the resistivity measurements. The labels "down" and "up" denotes decreasing and increasing H [or T], respectively, for the $\rho(H)$ [or $\rho(T)$] measurements.

4.2 Behaviour in the Magnetically Ordered States

Although the specific nature of each of the magnetically-ordered regions in the phase diagram of Fig. 4.3 is unknown, it is insightful to compare the transport and thermodynamic properties of CePtPb in these ordered regions to CePdAl [Fig. 1.8(b)] and YbAgGe [Fig. 1.7(b)] to determine where this compound sits in the family of the field-tuned antiferromagnets that have quasi-Kagome lattices for the rare-earth ions. Hysteresis is observed in $\rho(T, H)$ in the two intermediate phases of CePtPb between 0.8 and 3.5 kOe. Similarly, hysteresis in $\rho(T, H)$ is also observed in the two intermediate phases (phase B and C) [Fig. 1.8(b)] situated next to the zero-field phase (phase A) in CePdAl. It was speculated in [22] that phase B and C in CePdAl are canted AFM phases with spin flip-flop transitions at the phase boundaries AB and BC. This speculation is based on the Ising-like character of the Ce-$4f$ spins in phase A, which is inferred from the large magnetic anisotropy in zero field. Based on the same argument, there is a possibility that the intermediate phases with hysteresis in CePtPb are also canted AFM phases, given that a large magnetic anisotropy is also observed in the magnetic susceptibility at $H = 1$ kOe. On the other hand, hysteresis in $\rho(T, H)$ has only been observed in the zero-field phase (phase I) of YbAgGe [13, 14]. The zero-field phase of CePtPb doesn't exhibit any hysteresis in $\rho(T, H)$, suggesting the underlying magnetism in the zero-field phase of YbAgGe is different from CePtPb.

Furthermore, a power law analysis $\rho(T) = \rho_0 + AT^n$ of the electrical resistivity in zero field between 0.4 and 0.9 K has yielded an anomalous $n \approx 3$ exponent [Fig. 3.6(b) inset]. By plotting $\rho(T)$ versus T^3 for various applied fields as shown in Fig. 4.4, similar $n \approx 3$ dependence is found in all of the magnetically ordered phases in CePtPb. This $n \approx 3$ behaviour has also been reported in all of the magnetically ordered phases of CePdAl [22], but has not been reported for YbAgGe.

4.3 Behaviour in the Paramagnetic State

The power-law analysis $\rho(T) = \rho_0 + AT^n$ of the electrical resistivity for CePtPb in the paramagnetic region for $H \geq H_c$ indicates an anomalous evolution of the exponent n as a function of H. The fitting curves for representative values of the applied fields are shown in Figs. 4.5(a), (b), and (c). The data are fit in the temperature interval [0.4 K, T_{max}], where T_{max} grows with applied field as shown in the inset of Fig. 4.5(e). The values of ρ_0 are plotted together with the $\rho(H)$ data at $T = 0.4$ K [Fig. 4.5(d)] to show that the fitted ρ_0 agrees with the $\rho(H)$ data for $H \geq 20$ kOe. The value of n [Fig. 4.5(e)] increases continuously from $n = 2.5$ at $H = 7$ kOe to $n = 4.1$ at $H = 90$ kOe, and shows a tendency towards saturation near the value $n \approx 4$ for $H > 30$ kOe.

A similar enhancement of the resistivity exponent n by applied magnetic field is also observed in CeAuSb$_2$ [39] and CeNiGe$_3$ [67]. In CeAuSb$_2$, an exponent $n \approx 1$ was observed below 3 K near a critical applied field $H_c = 55$ kOe. As the applied field is increased, the
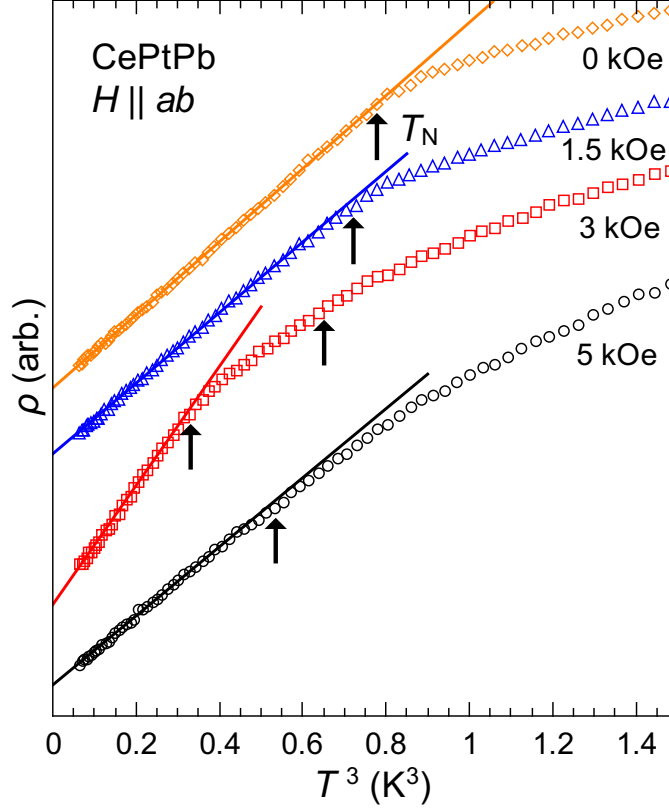
Figure 4.4: The electrical resistivity versus T^3 for CePtPb at low applied magnetic field in the magnetically-ordered state. These data were taken while sweeping down in temperature. The arrows indicate the Néel temperature T_N found in Section 4.1 through an analysis of $d\rho/dT$. The solid lines are linear fits to the plotted data below T_N.

exponent n grows rapidly and saturates to $n = 3$ near $H = 70$ kOe. For $H > 70$ kOe, the temperature range where this $n = 3$ behaviour is observed appears to increase linearly with increasing applied field, up to at least $H = 250$ kOe. It was speculated in [39] that the saturation to $n = 3$ is related to the alignment of the Ce-$4f$ spins, because both the resistivity exponent n and the magnetization appear to saturate at about the same field at a temperature $T < T_N$. In CeNiGe$_3$, the value of n grows from $n = 2$ at $H_c = 30$ kOe to $n \approx 3.8$ at $H = 90$ kOe, and continuous to grows markedly without signs of saturation.

In comparison to CeAuSb$_2$, the resistivity exponent n for CePtPb shows very similar behaviour. Firstly, the exponent n in both compounds grows rapidly and saturates at high values of the applied field. Secondly, the temperature interval where the saturation of n is observed increases linearly with applied field in both compounds. However, it is unclear why CePtPb shows a saturation value $n \approx 4$, whereas saturation $n = 3$ is observed in CeAuSb$_2$.

The value of A shows divergent behaviour near the critical field $H_c \approx 7$ kOe [Fig. 4.5(f)], as H is decreased from $H = 90$ kOe. Such divergent behaviour of A has been observed in
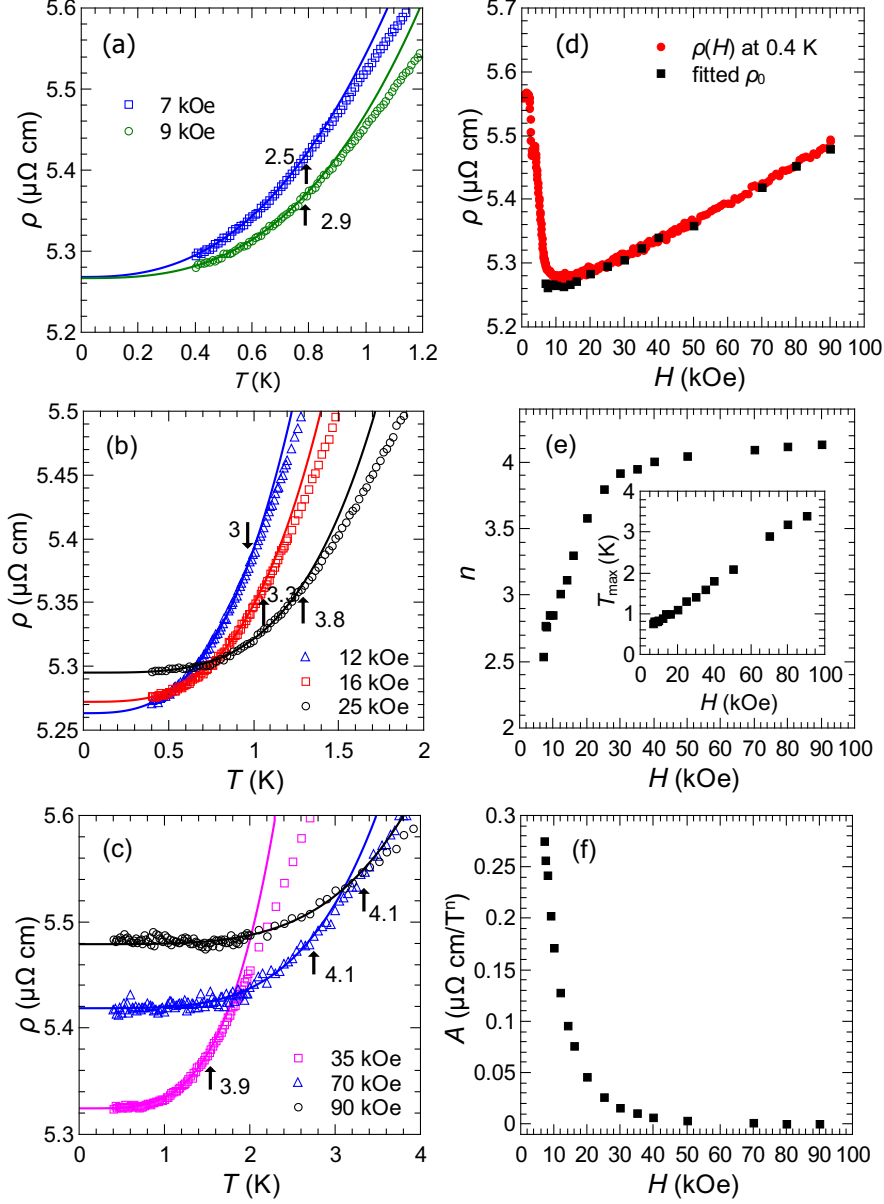
Figure 4.5: The power-law analysis, $\rho(T) = \rho_0 + AT^n$, of the electrical resistivity for CePtPb between 7 and 90 kOe. Graphs (a) to (c) show the fits of the data near the critical applied magnetic field $H_c = 7$ kOe, at intermediate fields, and at high fields, respectively. The data are fits in the temperature interval [0.4 K, T_{max}], where T_{max} is indicated by the arrows and the values of n listed beside them. The fitted values of the parameters are shown in (d) to (f).

several heavy-fermion compounds [13, 39, 22] (with $n = 2$) and has been attributed to proximity to a quantum critical point.

The anomaly observed in $C_m(T)$ for $H \geq H_c$ [Fig. 3.10(b)] shifts to higher temperatures as the applied field increases. The field-dependent behaviour of this anomaly can be
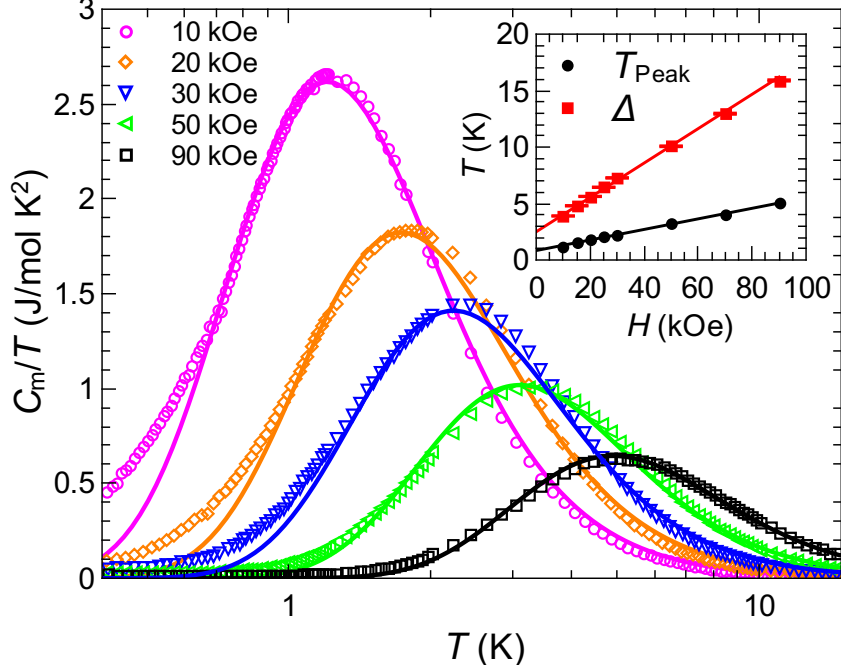
Figure 4.6: The magnetic contribution to the specific heat for CePtPb in the paramagnetic state for different magnetic fields $H \geq 10$ kOe applied in *ab*-plane. The data can be qualitatively fitted to a two-level Schottky anomaly model with an energy difference Δ. The magnetic field dependence of the peak temperature T_{peak} for this anomaly and Δ are plotted in the inset, where the lines are linear fits to the data.

attributed to an electronic Schottky contribution $C_{\text{Sch}}(T)$, associated with Zeeman splitting of the ground state CEF doublet. The Schottky contribution is given by

$$C_{\text{Sch}}(T) = \frac{k_{\text{B}} \Delta^2 e^{\Delta/T}}{T^2 [e^{\Delta/T} + 1]^2}, \tag{4.1}$$

where k_{B} is the Boltzmann constant and $k_{\text{B}}\Delta$ is the energy difference between the two CEF energy levels in the doublet [Fig. 4.6]. A reasonably good fit of the temperature dependence of $C_{\text{m}}(T)$ is achieved in the higher temperature region of the anomaly. At low temperatures, there is a clear discrepancy between the fit and the data, suggesting there is an additional contribution to $C_{\text{m}}(T)$ unaccounted for by the fit. This is discussed in the next section. The inset of Fig. 4.6 shows that the temperature of the peak in the anomaly T_{Peak} and the fitted value of Δ increase linearly with increasing magnetic field. This is consistent with a Zeeman splitting of the ground-state CEF doublet.

4.4 Behaviour Near the Critical Applied Magnetic Field

When the electronic Schottky contribution to the specific heat $C_{\mathrm{Sch}}(T)$ is subtracted from the magnetic contribution to the specific heat $C_{\mathrm{m}}(T)$, an additional contribution to $C_{\mathrm{m}}(T)$ is observed as a broad peak. This peak is shown in a $(C_{\mathrm{m}} - C_{\mathrm{Sch}})/T$ plot in the inset of Fig. 4.7. When the applied field increases, this peak shifts to higher values of temperature and broadens. Signatures of NFL behaviour, such as a $-\log T$ dependence, are not observed near the critical applied field $H_{\mathrm{c}} = 7$ kOe. At $T = 0.4$ K and $H = H_{\mathrm{c}}$, $(C_{\mathrm{m}} - C_{\mathrm{Sch}})/T$ has a large value of 0.56 J/mol K^2 that rapidly decreases with increasing applied field, as shown in the main panel of Fig. 4.7. This behaviour is typical for heavy-fermion systems, and is due to a suppression of the Kondo effect or the presence of short-range AFM correlations.
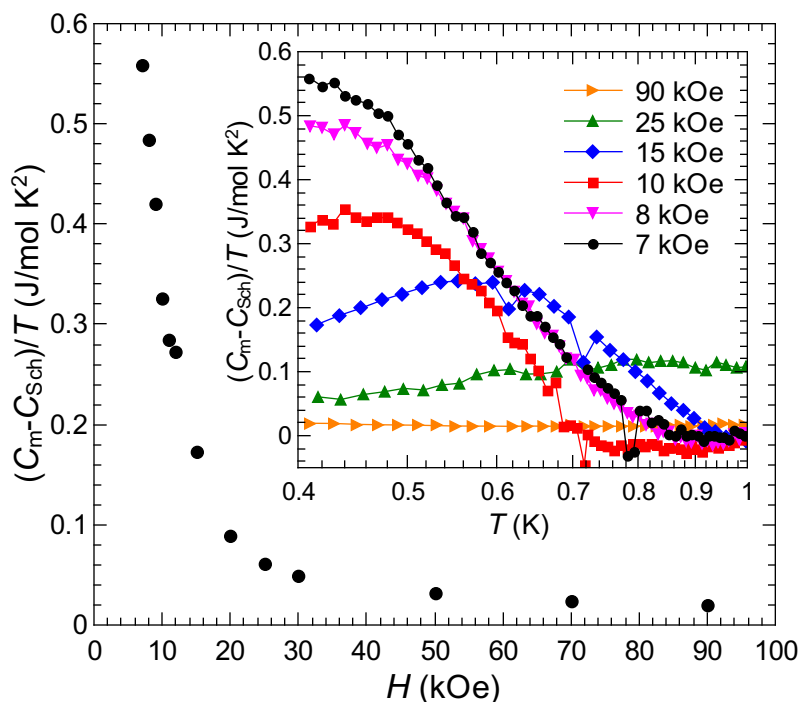
Figure 4.7: The magnetic field dependence of $(C_{\mathrm{m}} - C_{\mathrm{Sch}})/T$ for CePtPb at $T = 0.4$ K. The inset shows the temperature dependence of $(C_{\mathrm{m}} - C_{\mathrm{Sch}})/T$ for different magnetic fields applied in the ab-plane. The data points are connected by lines.

4.5 Interpretation of μSR Results

In the paramagnetic state of CePtPb [Fig. 3.15(b)], the ZF exponential relaxation rate λ associated with the Ce-4f moments increases as the temperature is lowered towards T_{N}. This is due to slowing down of the Ce-4f spin fluctuations that causes fluctuations of the local field component perpendicular to the initial muon spin polarization. Below T_{N}, where

the sample contribution to the ZF asymmetry spectra $A(t)$ develops two components [Fig. 3.15(a)], the amplitude of the slow-relaxing exponential component decreases smoothly to 37 % of the total sample asymmetry A_S at 25 mK. The corresponding relaxation rate λ_1 decreases with decreasing temperature to a non-zero value of 0.25 μs^{-1} at 25 mK [Fig. 3.15(b)]. The sharp rise in λ at T_N and fall of λ_1 below T_N indicates a peak that is consistent with critical slowing down of the Ce-$4f$ spin fluctuations when T_N is approached from the paramagnetic state and gradual slowing down when CePtPb is cooled below T_N. The non-zero value of the relaxation rate $\lambda_1 = 0.25$ μs^{-1}, however, suggests that slow Ce-$4f$ spin fluctuations persist in part of the sample.

In contrast to A_1, the amplitude A_2 of the ZF fast-relaxing exponential component grows below T_N to a value of 63 % of A_S at 25 mK [Fig. 3.15(a)]. Likewise the corresponding relaxation rate λ_2 increases to the large value 17 μs^{-1} [Fig. 3.15(c)], which is indicative of a broad internal magnetic field distribution.

The temperature dependences of A_1 and A_2 below T_N are compatible with two different scenarios. The first scenario is that there is a gradual Ce-$4f$ spin reorientation with decreasing temperature, such that the orientation of the average local field with respect to the initial muon spin polarization $\mathbf{P}(0)$ changes with decreasing temperature. The second, and more likely scenario, is that inhomogeneous freezing occurs below T_N, where part of the total volume contains Ce-$4f$ spins that do not freeze. These spins contribute a slowly relaxing signal component and hence are associated with the first term of Eq. (3.7). Conversely, the fast relaxing component of Eq. (3.7) is due to frozen spins. The amplitude A_1 and A_2 are dependent on the volume of the sample containing unfrozen and frozen spins, respectively. Hence the increase of the frozen spin volume (A_2) with decreasing temperature, comes at the expense of a diminished unfrozen spin volume (A_1). At 25 mK, $A_2/A_S = 63$ % and $A_1/A_S = 37$ %. The second scenario appears to be consistent with the magnetic structure proposed for CePdAl [48, 49], where 2/3 of the Ce-$4f$ spins order antiferromagnetically and the other 1/3 of the spins remains fluctuating.

In a longitudinal magnetic field applied in the *ab*-plane [Fig. 3.16(a)], the ratio of A_2/A_S at $T = 25$ mK increases slightly to 69 % at $H = 1$ kOe, but is drastically reduced to 15 % at $H = 3$ kOe. The higher A_2/A_S ratio at $H = 1$ kOe is consistent with a partial alleviation of the magnetic frustration by the applied field, which agrees with an earlier neutron diffraction study of CePdAl [52]. The lower A_2/A_S ratio at $H = 3$ kOe though is likely due to a Ce-$4f$ spin reorientation, because a phase boundary is apparently crossed when the magnetic field is increased from 1 to 3 kOe (see Fig. 4.3). The peak in $\lambda_1(T)$ in zero field shifts to lower temperatures due to suppression of T_N by the applied field [Fig. 3.16(b)]. The absence of a peak in $\lambda_1(T)$ for $H \geq 7$ kOe is consistent with the critical applied field $H_c \approx 7$ kOe extrapolated from the electrical resistivity measurements. The significant drop in λ_1 between 0 and 1 kOe for $T < T_N$ is also consistent with magnetic frustration being lifted as previously stated. On the other hand, as shown in Fig. 3.16(c),

$\lambda_2(T)$ is suppressed towards zero with increasing LF. This is because the LF competes with the internal magnetic field distribution and dominates at higher field.

Chapter 5

Conclusion

To date, studies of quantum critical behaviour in magnetically-frustrated heavy-fermion systems have primarily been restricted to non-metallic compounds. The addition of conduction electrons in the metallic systems further complicates the interplay between the $4f$-moments and has opened up a brand new field of physics. In this thesis, single crystals of CePtPb were grown from a Pb-rich solution and the crystal structure was characterized by Laue and powder X-ray diffraction measurements. A temperature-versus-magnetic field phase diagram constructed from electrical resistivity and specific heat measurements suggests several magnetically-ordered phases that terminate at a zero-temperature extrapolated critical applied magnetic field $H_c \approx 7$ kOe. The specific nature of each magnetically-ordered phase is uncertain, which warrants neutron diffraction measurements in the future. Nevertheless, some insight into the nature of these phases could be obtained by μSR.

The ZF-μSR measurements indicate residual spin dynamics at 25 mK, consistent with the magnetic structure proposed for the related compound CePdAl, where 2/3 of the Ce-$4f$ spins order antiferromagnetically and the other 1/3 of the Ce-$4f$ spins remain fluctuating due to geometric frustration. In the future, μSR experiments with a weak magnetic field applied transverse to the initial muon spin polarization $\mathbf{P}(0)$ could potentially confirm whether there is phase separation in the sample at $T < T_N$ associated with frozen and unfrozen spins.

Similar to CePdAl, neither Fermi-liquid (FL) nor non-Fermi-liquid (NFL) behaviour is observed for $H \geq H_c$ [22, 53]. Instead, the electrical resistivity of each compound exhibits a power-law dependence on temperature with exponent $n > 2$ in both the magnetically-ordered and paramagnetic states. On the other hand, NFL behaviour is observed near a critical field $H_c = 45$ kOe in YbAgGe that extends over a wide field range to $H = 105$ kOe before FL behaviour is recovered at higher fields [13, 16]. It is speculated that the physics driving the ground state of the Ce- and Yb-based compounds is slightly different. In the future, it will be interesting to study the quantum critical behaviour of CePdPb, which is another compound with the Ce-$4f$ moments occupying quasi-Kagome lattices in the *ab*-plane. An earlier study [68] concluded that CePdPb does not ordered magnetically down to

$T = 3$ K, but estimated a Curie-Weiss temperature $\theta_{\mathrm{CW}} = -35$ K that suggests an AFM ground state for this compound. Hence, this may be another magnetically frustrated AFM compound, which could provide further insight into the physics driving the ground state of CePtPb with the replacement of only one constituent element (i.e., Pd rather than Pt).

In CePtPb, the exponent n of the temperature-dependent electrical resistivity for $H \geq H_{\mathrm{c}}$ shows an anomalous increase with field and saturates to an exponent $n \approx 4$ for $H > 30$ kOe. Similar behaviour has also been observed in CeAuSb$_2$ [39] and CeNiGe$_3$ [67] with different saturation exponents. In CeAuSb$_2$, the saturation to $n = 3$ is speculated [39] to be related to the alignment of the Ce-$4f$ spins, because both the magnetization and n saturates at the same applied field. This agreement between the magnetization and n should also be investigated for CePtPb. A density functional theory calculation of the electrical resistivity [69] for different lattices with fully polarized Ce-$4f$ spins might provide insight to the different observed saturation exponents.

Bibliography

[1] C. Kittel, and P. McEuen, *Introduction to Solid State Physics* (Wiley, New York, 1996), Vol. 8.

[2] E. Borchi, and S. DeGennaro, J. Phys. F: Metal Phys. **10**, 271 (1980).

[3] J. Flouquet, J. C. Lasjaunias, J. Peyrard, and M. Ribault, J. Appl. Phys. **53**, 3 (1982).

[4] K. Andres, J. E. Graebner, and H. R. Ott, Phys. Rev. Lett. **35**, 26 (1975).

[5] K. R. Shirer, A. C. Shockley, A. P. Dioguardi, J. Crocker, C. H. Lin, D. M. Nisson, P. Klavins, J. C. Cooley, Y.-F. Yang, and N. J. Curro, *PNAS* **109**, 45 (2012).

[6] D. T. Adroja and S. K. Malik, J. Magn. Magn. Mater. **100**, 126-138 (1991).

[7] F. M. Grosche, I. R. Walker, S. R. Julian, N. D. Mathur, D. M. Freye, M. J. Steiner, and G. G. Lonzarich, J. Phys. Condens. Matter **13**, 2845-2860 (2001).

[8] G. Knebal, D. Braithwaite, P. C. Canfield, G. Lapertot, and J. Flouquet, High Press. Res. **22**, 167-170 (2002).

[9] N. D. Mathur, F. M. Grosche, S. R. Julian, I. R. Walker, D. M. Freye, R. K. W. Haselwimmer, and G. G. Lonzarich, Nature **394**, 39-43 (1998).

[10] S. Doniach, Physica B+C **91**, 231-234 (1977).

[11] T. Pietrus, B. Bogenberger, S. Mock, M Sieck, and H. v. Löhneysen, Physica B Condens. Matter **206**, 317-319 (1995).

[12] J. Custers, P. Gegenwart, H. Wilhelm, K. Neumaier, Y. Tokiwa, O. Trovarelli, C. Geibel, F. Steglich, C. Pépin, and P. Coleman, Nature **424**, 524 (2003).

[13] S. L. Bud'ko, E. Morosan, and P. C. Canfield, Phys. Rev. B **69**, 014415 (2004).

[14] K. Umeo, K. Yamane, Y. Muro, K. Katoh, Y. Niide, A. Ochiai, T. Morie, T. Sakakibara, and T. Takabatake, J. Phys. Soc. Jpn. **73**, 537-540 (2004).

[15] E. Morosan, S. L. Bud'ko, P. C. Canfield, M. S. Torikachvili, and A. H. Lacerda, J. Magn. Magn. Mater. **277**, 298-321 (2004).

[16] E. Mun, S. L. Bud'ko, and P. C. Canfield, Phys. Rev. B **82**, 174403 (2010).

[17] G. M. Schmiedeshoff, E. Mun, A. W. Lounsbury, S. J. Tracy, E. C. Palm, S. T. Hannahs, J.-H. Park, T. P. Murphy, S. L. Bud'ko, and P. C. Canfield, Phys. Rev. B **83**, 180408 (2011).

[18] Y. Tokiwa, M. Garst, P. Gegenwart, S. L. Bud'ko, and P. C. Canfield, Phys. Rev. Lett. **111**, 116401 (2013).

[19] T. Park, V. A. Sidorov, F. Ronning, J.-X. Zhu, Y. Tokiwa, H. Lee, E. D. Bauer, R. Movshovich, J. L. Sarrao, and J. D. Thompson, Nature **456**, 366 (2008).

[20] D. M. Fobes, E. D. Bauer, J. D. Thompson, A. Sazonov, V. Hutanu, S. Zhang, F. Ronning, and M. Janoschek, J. Phys. Condens. Matter **29**, 17LT01 (2017).

[21] S. T. Bramwell and M. J. P. Gingras, Science **294**, 1495-1501 (2001).

[22] H. Zhao, J. Zhang, S. Hu, Y. Isikawa, J. Luo, F. Steglich, and P. Sun, Phys. Rev. B **94**, 235131 (2016).

[23] J. Kondo, Prog. Theor. Phys. **32**, 37-49 (1964).

[24] V. T. Rajan, Phys. Rev. Lett. **51**, 308 (1983).

[25] W. J. de Haas, J. de Boer, and G. J. van dën Berg, Physica **1**, 1115-1124 (1934).

[26] A. N. Gerritsen and J. O. Linde, Physica **18**, 877-890 (1952).

[27] T. H. Blewitt, R. R. Coltman Jr., and J. K. Redman, Phys. Rev. **93**, 891 (1954).

[28] A. C. Hewson, *The Kondo Problem to Heavy Fermions* (Cambridge University Press, 1997), Vol. 2.

[29] P. Coleman, Heavy Fermion: Electrons at the Edge of Magnetism, *Handbook of Mangetism and Advanced Magnetic Materials* (John Wiley & Sons, 2007).

[30] M. A. Ruderman and C. Kittel, Phys. Rev. **96**, 99 (1954).

[31] T. Kasuya, Prog. Theor. Phys. **16**, 45-57 (1956).

[32] K. Yosida, Phys. Rev. **106**, 893 (1957).

[33] F. Steglich, J. Arndt, O. Stockert, S. Friedemann, M. Brando, C. Klingner, C. Krellner, C. Geibel, S. Wirth, S. Kirchner *et. al.*, J. Phys. Condens. Matter **24**, 294201 (2012).

[34] G. R. Stewart, Rev. Mod. Phys. **73**, 797 (2001).

[35] G. R. Stewart, Rev. Mod. Phys. **78**, 743 (2006).

[36] J. A. Hertz, Phys. Rev. B **14**, 1165 (1976).

[37] A. J. Millis, Phys. Rev. B **48**, 7183 (1993).

[38] T. Moriya and T. Takimoto, J. Phys. Soc. Jpn. **64**, 960-969 (1995).

[39] L. Balicas, S. Nakatsuji, H. Lee, P. Schlottmann, T. P. Murphy, and Z. Fisk, Phys. Rev. B **72**, 064422 (2005).

[40] L. Balents, Nature **464**, 199 (2010).

[41] G. H. Wannier, Phys. Rev. **79**, 257 (1950).

[42] K. Kano and S. Naya, Prog. Theor. Phys. **10**, 158-172 (1953).

[43] R. J. Szabo, J. Phys. Conf. Ser. **95**, 012401 (2018).

[44] Y. Machida, S. Nakatsuji, S. Onoda, T. Tayama, and T. Sakakibara, Nature **463**, 210 (2010).

[45] J. A. Sears, M. Songvilay, K. W. Plumb, J. P. Clancy, Y. Qiu, Y. Zhao, D. Parshall, and Y.-J. Kim, Phy. Rev. B. **91**, 144420 (2015).

[46] P. Coleman and A. H. Nevidomskyy, J. Low Temp. Phys. **161**, 182-202 (2010).

[47] B. Fåk, D. F. McMorrow, P. G. Niklowitz, S. Raymond, E. Ressouche, J. Flouquet, P. C. Canfield, S. L. Bud'ko, Y. Janssen, and M. J. Gutmann, J. Phys. Condens. Matter **17**, 301 (2004).

[48] V. Fritsch, S. Lucas, Z. Huesges, A. Sakai, W. Kittler, C. Taubenheim, S. Woitschach, B. Pedersen, K. Grube, B. Schmidt *et. al.*, J. Phys. Conf. Ser. **807**, 032003 (2017).

[49] A. Dönni, G. Ehlers, H. Maletta, P. Fischer, H. Kitazawa, and M. Zolliker, J. Phys. Condens. Matter **8**, 11213 (1996).

[50] S. Woitschach, O. Stockert, M. M. Koza, V. Fritsch, H. v. Löhneysen, and F. Steglich, Phys. Status Solidi B **250**, 468-471 (2013).

[51] A. Oyamada, S. Maegawa, M. Nishiyama, H. Kitazawa, and Y. Isikawa, Phys Rev. B **77**, 064432 (2008).

[52] K. Prokeš, P. Manuel, D. T. Adroja, H. Kitazawa, T. Goto, and Y. Isikawa, Physica B: Condens. Matter **385**, 359-362 (2006).

[53] S. Lucas, K. Grube, C.-L. Huang, A. Sakai, S. Wunderlich, E. L. Green, J. Wosnitza, V. Fritsch, P. Gegenwart, O. Stockert *et. al.*, Phys. Rev. Lett. **118**, 107204 (2017).

[54] R. Movshovich, J. M. Lawrence, M. F. Hundley, J. Neumeier, J. D. Thompson, A. Lacerda, and Z. Fisk, Phys. Rev. B **53**, 5465 (1996).

[55] H. Okamoto, *Desk Handbook: Phase Diagrams for Binary Alloys* (ASM International, 2000), Vol. 314.

[56] G. J. Sellers and A. C. Anderson, Rev. Sci. Instrum. **45**, 1256-1259 (1974).

[57] G. R. Stewart, Rev. Sci. Instrum. **54**, 1-11 (1983).

[58] R. Kubo and T. Toyabe, *Magnetic Resonance and Relaxation* (North-Holland, Amsterdam, 1967).

[59] S. L. Lee, R. Cywinski, and S. H. Kilcoyne, *Muon Science: Muons in Physics, Chemistry and Materials* (CRC Press,1999), Vol. 51.

[60] R. S. Hayano, Y. J. Uemura, J. Imazato, N. Nishida, T. Yamazaki, and R. Kubo, Phys. Rev. B **20**, 850 (1979).

[61] P. D. de Réotier, and A. Yaouanc, J. Phys. Condens. Matter **4**, 4533 (1992).

[62] F. Shibata, and Y. S, Physica A **215**, 87-103 (1995).

[63] J. Rodríguez-Carvajal, EdPCR manual, FULLPROF Laboratoire Leon Brillouin, 2001.

[64] G. T. Furukawa, W. G. Saba, and M. L. Reilly, Technical Report, National Standard Reference Data System, 1968.

[65] D. W. Bloom, D. H. Lowndes Jr., and L. Finegold, Rev. Sci. Instrum. **41**, 690-695 (1970).

[66] W. K. Robinson and S. A. Friedberg, Phys. Rev. **117**, 402 (1960).

[67] E. Mun, S. L. Bud'ko, A. Kreyssig, and P. C. Canfield, Phys. Rev. B **82**, 054424 (2010).

[68] W. Hermes, S. Rayaprol, and R. Poettgen, Z. Naturforsch. B Chem. Sci. **62**, 901-907 (2007).

[69] D. Alfe, M. Pozzo, M. P. Desjarlais, Phys. Rev. B **85**, 024102 (2012).